EUMETSAT
AC SAF
ATMOSPHERIC COMPOSITION
MONITORING

ALGORITHM THEORETICAL BASIS DOCUMENT

GOME-2 surface LER product

Product Identifier	Product Name
O3M-402	Surface LER from GOME-2 / MetOp-A+B

Authors	Institute
L.G. Tilstra	Royal Netherlands Meteorological Institute (KNMI)
O.N.E. Tuinder	Royal Netherlands Meteorological Institute (KNMI)
P. Stammes	Royal Netherlands Meteorological Institute (KNMI)

Document status sheet

Issue	Date	Page(s)	Modified Items / Reason for Change
0.1	20-11-2012	all	first draft version
0.2	22-01-2013	all	second draft version ; document complete
1.0	18-03-2013	all	first official version of document
1.1	23-10-2013	21	added solar eclipse filtering ; added appendices A and B
1.2	25-11-2013	all	changes and update after RR/PCR
1.3	12-12-2013	7,12	further changes after RR/PCR
1.4	02-04-2014	all	added O3M-90 ; update of figures ; textual changes
1.5	25-06-2014	11,13	changes and update after DRR
1.6	13-11-2014	7	added "Heritage" section (1.2)
1.7	26-10-2015	all	extended section 6 ; updated section 1.5 and tables 1,2,5,6
2.0	24-11-2016	all	added new section 5 ; updated section 3.4.1 and tables 5,6
2.1	20-12-2016	all	changes and update after RR/PCR
2.2	02-05-2017	7,8	minor changes and update after DRR
3.0	26-09-2018	all	added new section 6 ; extended and updated sections 1–3,5,7,8 ; added figures 1,9–14,16 ; updated tables 1–3,5,6
3.1	25-03-2019	all	changes and update after DRR ; added new sections 1.4, 4.1 and 6.5 ; renamed sections 3, 3.6 and 4 ; updated appendix B

Contents

Introduction to EUMETSAT Satellite Application Facility on Atmospheric Composition monitoring (AC SAF)

Background

The monitoring of atmospheric chemistry is essential due to several human caused changes in the atmosphere, like global warming, loss of stratospheric ozone, increasing UV radiation, and pollution. Furthermore, the monitoring is used to react to the threads caused by the natural hazards as well as follow the effects of the international protocols.

Therefore, monitoring the chemical composition and radiation of the atmosphere is a very important duty for EUMETSAT and the target is to provide information for policy makers, scientists and general public.

Objectives

The main objectives of the AC SAF is to process, archive, validate and disseminate atmospheric composition products (O_3, NO_2, SO_2, BrO, HCHO, H_2O, OClO, CO, NH_3), aerosol products and surface ultraviolet radiation products utilising the satellites of EUMETSAT. The majority of the AC SAF products are based on data from the GOME-2 and IASI instruments onboard MetOp satellites.

Another important task besides the near real-time (NRT) and offline data dissemination is the provision of long-term, high-quality atmospheric composition products resulting from reprocessing activities.

Product categories, timeliness and dissemination

NRT products are available in less than three hours after measurement. These products are disseminated via EUMETCast, WMO GTS or internet.

- Near real-time trace gas columns (total and tropospheric O_3 and NO_2, total SO_2, total HCHO, CO) and ozone profiles
- Near real-time absorbing aerosol indexes from main science channels and polarisation measurement detectors
- Near real-time UV indexes, clear-sky and cloud-corrected

Offline products are available within two weeks after measurement and disseminated via dedicated web services at EUMETSAT and AC SAF.

- Offline trace gas columns (total and tropospheric O_3 and NO_2, total SO_2, total BrO, total HCHO, total H_2O) and ozone profiles
- Offline absorbing aerosol indexes from main science channels and polarisation measurement detectors
- Offline surface UV, daily doses and daily maximum values with several weighting functions

Data records are available after reprocessing activities from the EUMETSAT Data Centre and/or the AC SAF archives.

- Data records generated in reprocessing
- Surface Lambertian-equivalent reflectivity
- Total OClO

Users can access the AC SAF offline products and data records (free of charge) by registering at the AC SAF web site.

More information about the AC SAF project, products and services: http://acsaf.org/

AC SAF Helpdesk: helpdesk@acsaf.org

Twitter: https://twitter.com/Atmospheric_SAF

1   Introduction

1.1   Document purpose and scope

This document is the Algorithm Theoretical Basis Document (ATBD) for the GOME-2 surface LER products developed at KNMI in the framework of the AC SAF (Satellite Application Facility on Atmospheric Composition Monitoring). The aim of this ATBD is to present the scientific background of the algorithm and to provide a description of the algorithm setup.

1.2   Heritage

The GOME-2 surface LER product is the Lambertian-equivalent reflectivity (LER) of the Earth's surface observed by the GOME-2 instruments. It is the improved follow-up of earlier surface LER databases based on observations performed by GOME-1 (on the ERS-2 satellite) [*Koelemeijer et al.*, 2003] and OMI (on the Aura satellite) [*Kleipool et al.*, 2008].

The GOME-2 surface LER products are developed at KNMI in the framework of the AC SAF (Satellite Application Facility on Atmospheric Composition Monitoring). The algorithm described in section 3 of this ATBD is the direct continuation of the algorithms that were developed by *Koelemeijer et al.* [2003] and *Kleipool et al.* [2008]. Also see *Tilstra et al.* [2017].

1.3   GOME-2 surface LER product

Only one GOME-2 surface LER product is produced. Previously, separate products were produced for each GOME-2 instrument. The current product is based on the combination of level-1 data from the GOME-2 instruments on the MetOp-A and MetOp-B satellites. To be more specific:

Product ID	Satellite	Platform	Surface LER versions
O3M-402	GOME-2	MetOp-A + MetOp-B	MSC & PMD

The GOME-2AB surface LER product consists of two surface LER versions: one version based on GOME-2 observations by the Main Science Channels (MSCs) and one version based on GOME-2 observations by the Polarisation Measurement Devices (PMDs). The PMD-based version has the advantage over the MSC-based version that the surface LER is based on eight times as many observations, each with an eight times smaller footprint. This makes the retrieved surface LER less susceptible to residual cloud contamination, statistically more stable, and therefore more reliable. It also allows a higher spatial resolution of the intrinsic surface LER database grid.

On the other hand, the surface LER of the PMD-based version is available only for a fixed list of wavelength bands. The wavelengths of the PMD bands are given in Table 3. This limitation is not an issue for the MSC-based surface LER. Here the list of wavelength bands could be determined based on user needs, taking into account that the wavelength bands have to be positioned in the continuum, avoiding strong absorption bands. The selected wavelength bands are given in Table 2. In this ATBD we do not distinguish between the two approaches, because they are very similar.

1.4   General layout of algorithm and document

The data processor consists of several steps and components, which are each described in a separate section of this ATBD. The basic surface LER algorithm is described in section 3. Post-processing corrections are described in section 4. These two steps already result in a complete surface LER database and basically describe the baseline of the release of O3M-89 in the year 2014. The actions needed to increase the spatial resolution of the databases via the concept of dynamic gridding are described in section 5. Up to this point this agrees more or less with the baseline that was used for the previous releases O3M-89.1 and O3M-90 in the year 2017. Finally, section 6 describes the algorithm extension that determines the directionally dependent Lambertian-equivalent reflectivity (DLER) of the Earth's surface. To summarise the steps and their associated sections in this ATBD:

1. Basic surface LER retrieval → section 3

2. Post-processing corrections and flags → section 4

3. Dynamic gridding → section 5

4. Creating the directional LER database (DLER) → section 6

Algorithm steps (3) and (4), described in sections 5 and 6, respectively, are making use of algorithm steps (1) and (2), described in sections 3 and 4, respectively, by running these algorithm steps for different spatial resolutions and/or for different viewing angle regimes.

1.5   Suggested reading material

Herman, J. R., and E. A. Celarier (1997), Earth surface reflectivity climatology at 340–380 nm from TOMS data, *J. Geophys. Res., 102*(D23), 28,003–28,011, doi:10.1029/97JD02074.

Koelemeijer, R. B. A., J. F. de Haan, and P. Stammes (2003), A database of spectral surface reflectivity in the range 335–772 nm derived from 5.5 years of GOME observations, *J. Geophys. Res., 108*(D2), 4070, doi:10.1029/2002JD002429.

Gao, F., C. B. Schaaf, A. H. Strahler, A. Roesch, W. Lucht, and R. Dickinson (2005), MODIS bidirectional reflectance distribution function and albedo Climate Modeling Grid products and the variability of albedo for major global vegetation types, *J. Geophys. Res., 110*, D01104, doi:10.1029/2004JD005190.

Kleipool, Q. L., M. R. Dobber, J. F. de Haan, and P. F. Levelt (2008), Earth surface reflectance climatology from 3 years of OMI data, *J. Geophys. Res., 113*, D18308, doi:10.1029/2008JD010290.

Popp, C., P. Wang, D. Brunner, P. Stammes, Y. Zhou, and M. Grzegorski (2011), MERIS albedo climatology for FRESCO+ O2 A-band cloud retrieval, *Atmos. Meas. Tech., 4*, 463–483, doi:10.5194/amt-4-463-2011.

Tilstra, L. G., O. N. E. Tuinder, P. Wang, and P. Stammes (2017), Surface reflectivity climatologies from UV to NIR determined from Earth observations by GOME-2 and SCIAMACHY, *J. Geophys. Res. Atmos., 122*, 4084–4111, doi:10.1002/2016JD025940.

Tilstra, L. G., O. N. E. Tuinder, P. Wang, and P. Stammes (2017), Surface albedo databases determined from PMD measurements performed by the GOME-2 instrument, *Proceedings of the 2017 EUMETSAT Meteorological Satellite Conference,* EUMETSAT, Rome, Italy, 2017.

1.6   Abbreviations and acronyms

AAH	Absorbing Aerosol Height
AAI	Absorbing Aerosol Index
AC SAF	Satellite Application Facility on Atmospheric Composition Monitoring
AOT	Aerosol Optical Thickness
ATBD	Algorithm Theoretical Basis Document
BBA	Biomass Burning Aerosol
BRDF	Bidirectional Reflectance Distribution Function
BSA	Black-Sky Albedo
CDOP	Continuous Development & Operations Phase
COT	Cloud Optical Thickness
DAK	Doubling-Adding KNMI
DOAS	Differential Optical Absorption Spectroscopy
DU	Dobson Units, 2.69×10^{16} molecules cm^{-2}
ENVISAT	Environmental Satellite
EOS-Aura	Earth Observing System – Aura satellite
ERS	European Remote Sensing Satellite
ESA	European Space Agency

ETOPO-4	Topographic & Bathymetric data set from the NGDC, 4 arc-min. resolution
EUMETSAT	European Organisation for the Exploitation of Meteorological Satellites
FOV	Field-of-View
FRESCO	Fast Retrieval Scheme for Clouds from the Oxygen A band
FWHM	Full Width at Half Maximum
GMTED2010	Global Multi-resolution Terrain Elevation Data 2010
GOME	Global Ozone Monitoring Experiment
HDF	Hierarchical Data Format
IT	Integration Time
KNMI	Koninklijk Nederlands Meteorologisch Instituut
LER	Lambertian-Equivalent Reflectivity
LUT	Look-Up Table
MERIS	Medium Resolution Imaging Spectrometer
METOP	Meteorological Operational Satellite
MLS	Mid-Latitude Summer
MSC	Main Science Channel
NGDC	NOAA's National Geophysical Data Center (Boulder, Colorado, USA)
NISE	Near-real-time Ice and Snow Extent
NOAA	National Oceanic and Atmospheric Administration
NRT	Near-Real-Time
OMI	Ozone Monitoring Instrument
O3M SAF	Satellite Application Facility on Ozone and Atmospheric Chemistry Monitoring
PMD	Polarisation Measurement Device
PSD	Product Specification Document
PUM	Product User Manual
RMSE	Root-Mean-Square Error
RTM	Radiative Transfer Model
SCIAMACHY	Scanning Imaging Absorption Spectrometer for Atmospheric Chartography
SZA	Solar Zenith Angle
TEMIS	Tropospheric Emission Monitoring Internet Service
TOA	Top-of-Atmosphere
TOMS	Total Ozone Mapping Spectrometer
UTC	Universal Time Co-ordinate
UV	Ultraviolet
VIS	Visible
VR	Validation Report
VZA	Viewing Zenith Angle

2 Surface reflectivity databases for the UV-VIS

2.1 Introduction

Surface reflectivity databases are needed for cloud, aerosol and trace gas retrievals. One of the first surface reflectivity databases retrieved using UV satellite remote sensing techniques is the Total Ozone Mapping Spectrometer (TOMS) [*Heath et al.*, 1975] surface LER database [*Herman and Celarier*, 1997]. The retrieved reflectivity is the Lambertian-equivalent reflectivity (LER) of the surface found from scenes which are assumed to be cloud free. The retrieval method relies on the removal of the (modelled) atmospheric contribution from the (observed) top-of-atmosphere (TOA) reflectance. In this approach the surface is defined to behave as a Lambertian reflector. The TOMS surface LER database ($1.25° \times 1°$) was retrieved for 340 and 380 nm only, which limits its usefulness.

The GOME [*Burrows et al.*, 1999] surface reflectivity database provides the surface LER on a $1° \times 1°$ grid for 11 wavelength bands between 335 and 772 nm [*Koelemeijer et al.*, 2003]. Although this is already quite an improvement with respect to the TOMS surface LER database, the database is still limited in quality by the low number of measurements from which the surface LER had to be extracted and the large GOME footprint size (see Table 1). In particular, pixels over sea are often affected by residual cloud contamination. In these cases the surface LER was retrieved from scenes which were not sufficiently cloud free. In other cases, e.g. snow surfaces, the surface LER was retrieved from a few measurements which were not representative for the entire month.

A large improvement on these points is the OMI surface reflectivity database [*Kleipool et al.*, 2008]. First, the OMI instrument [*Levelt et al.*, 2006] has a much smaller footprint size (24×13 km^2 at nadir) combined with a larger global coverage (see Table 1). This leads to better statistics and results in a higher accuracy for the surface LER retrieval. Second, the higher number of measurements allows for inspecting the distribution of scene LERs for each grid cell, and for making a more sophisticated selection of representative (cloud-free) scenes instead of directly taking the minimum scene LER value like in the case of the TOMS and GOME databases. Third, the provided OMI surface LER database has a higher spatial resolution ($0.5° \times 0.5°$ grid). The limiting factor is the OMI wavelength range. The longest wavelength in the OMI surface LER database is 499 nm.

The GOME-2 series of satellite instruments does not have some of the limitations of the satellite instruments mentioned above and can be used to create a better, more reliable surface LER database [*Tilstra et al.*, 2017]. To be more specific, it has the spectral range of GOME but a much smaller footprint (80×40 km^2) which is constant over the full swath width. Additionally, the number of measurements that are available per longitude/latitude cell is smaller than that of OMI, but enough to perform a statistical analysis on the distribution of retrieved scene LERs. Developing the GOME-2 surface LER retrieval the approach used for the OMI surface LER database was followed.

The main advantage of the GOME-2 surface LER database with respect to the OMI surface LER database is the wider wavelength range of the GOME-2 instrument. Additionally, the retrieval algorithm uses aerosol information, available via the GOME-2 Absorbing Aerosol Index (AAI) product, to filter out scenes with large aerosol loadings, as these scenes can result in inaccurate values of the retrieved surface LER. This filtering is especially important for locations over desert areas.

2.2 Tables

In Table 1 we summarise the properties of the discussed surface reflectivity databases. For GOME-2 we provide the specifications for the MSC-based and PMD-based algorithms. In Table 2 we list the wavelength bands of the surface reflectivity databases, and their application. In Table 3 we provide the wavelengths of the GOME-2 PMD bands, relevant to the PMD-based algorithm. The selection of the wavelength bands for the GOME-2 MSC-LER was influenced largely by the already existing surface LER databases. Below 325 nm the surface contribution to the TOA reflectance is low, which prevents an accurate retrieval of the surface LER below this wavelength. For the GOME-2 PMD-LER this means that the surface LER for PMDs 1–3 cannot be retrieved, as indicated.

instrument	TOMS	GOME	OMI	MSC - GOME-2 - PMD	
satellite	Nimbus-7	ERS-2	Aura	MetOp-A/B	
equator crossing time (LT)	12:00	10:30	13:45	09:30	
dayside flight direction	S→N	N→S	S→N	N→S	
number of days for global coverage	1	3	1	1.5	
pixel size at nadir (km × km)	50 × 50	320 × 40	24 × 13	80 × 40	10 × 40
number of usable pixels per orbit	∼12000	∼1300	∼83000	∼11000	∼88000
dataset time range [(*)]	1978–1993	1995–2000	2004–2007	2007–2018	2008–2018
selected wavelength bands	2	11	23	26	12
wavelength range covered (nm)	340–380	335–772	328–499	328–772	333–799
band width (nm)	1.0	1.0	1.0	1.0	see text
spatial resolution (°lon × °lat)	1.25 × 1.0	1.0 × 1.0	0.5 × 0.5	1.0 × 1.0	0.5 × 0.5
reference	HC1997	KHS2003	KDHL2008	TTWS2017	

Table 1: Characteristics and properties of the UV-VIS surface LER databases, and of the satellite instruments from which they are derived. Wavelength band information can be found in Tables 2/3.

[(*)]The longer the time period covered, the higher the number of times a certain region has been observed. This increases the chances of having observed this region under clear sky conditions. Occasional reprocessing over longer time periods therefore increases the quality, stability, and reliability of the surface LER product. GOME-2 data from MetOp-A are available from January 2007; GOME-2 data from MetOp-B are available since December 2012.

Table 2: Wavelength bands of the four monochromatic surface LER databases, and their applications. All wavelength bands are located outside strong gaseous absorption bands in order to avoid complicated modelling of the radiative transfer. The number of wavelength bands is also given.

λ (nm)	TOMS	GOME	OMI	GOME-2	application / relevance
328			+	+	LER, ozone, HCHO, SO$_2$
335		+	+	+	LER, ozone, HCHO
340	+			+	LER, aerosol, HCHO, BrO
342			+		LER, aerosol, HCHO, BrO
345			+		LER, aerosol, HCHO, BrO
354			+	+	LER, aerosol, HCHO, BrO, OClO
367			+	+	LER, aerosol, OClO
372			+		LER, aerosol, OClO
376			+		LER, aerosol, OClO
380	+	+	+	+	LER, aerosol, OClO
388			+	+	LER, aerosol, OClO
406			+		LER, aerosol
416		+	+	+	LER, aerosol
418			+		LER, aerosol
425			+	+	LER, aerosol, NO$_2$
440		+	+	+	LER, aerosol, NO$_2$
442			+		LER, aerosol, NO$_2$
452			+		LER, aerosol, NO$_2$
463		+	+	+	LER, aerosol, NO$_2$, O$_2$-O$_2$
471			+		LER, aerosol, NO$_2$, O$_2$-O$_2$
477			+		LER, aerosol, NO$_2$, O$_2$-O$_2$
488			+		LER, aerosol, NO$_2$, O$_2$-O$_2$
494		+	+	+	LER, aerosol, NO$_2$, O$_2$-O$_2$
499			+		LER, aerosol
510				+	LER, aerosol
526				+	LER, aerosol, vegetation
546				+	LER, aerosol, vegetation
555		+		+	LER, aerosol, vegetation
564				+	LER, aerosol, vegetation, O$_2$-O$_2$

λ					application / relevance
585				+	LER, aerosol, vegetation, O_2-O_2, H_2O
610		+		+	LER, aerosol, H_2O
640				+	LER, aerosol, H_2O
670		+		+	LER, aerosol, H_2O, O_2-B
685				+	LER, aerosol, H_2O, O_2-B
697				+	LER, aerosol, H_2O, O_2-B
712				+	LER, aerosol, H_2O, O_2-B
758		+		+	LER, aerosol, O_2-A
772		+		+	LER, aerosol, O_2-A
Total:	2	11	23	26	

Table 2: Wavelength bands of the four monochromatic surface LER databases, and their applications. All wavelength bands are located outside strong gaseous absorption bands in order to avoid complicated modelling of the radiative transfer. The number of wavelength bands is also given.

The widths of the PMD bands are not provided in Table 3, but these (and other information) can be found in the "GOME-2 Factsheet" [*EUMETSAT*, 2015]. Additionally, Figure 1 provides a graphical representation of the spectral response functions of the PMD bands. The spectral response functions were determined using the slit functions of the individual detector pixels that make up the PMD bands. Note that we use the data from the PMD-p detector, not from the PMD-s detector. Ideally, PMD-p and PMD-s detectors should provide the same reflectance. In practice, they do not.

PMD	λ (nm)	application / relevance	PMD	λ (nm)	application / relevance
01	313	not retrieved	09	461	LER, aerosol, NO_2, O_2-O_2
02	318	not retrieved	10	520	LER, aerosol
03	325	not retrieved	11	555	LER, aerosol, vegetation
04	333	LER, ozone, HCHO	12	590	LER, aerosol
05	338	LER, aerosol, HCHO, BrO	13	640	LER, aerosol, H_2O
06	369	LER, aerosol, OClO	14	757	affected by O_2 absorption
07	382	LER, aerosol, OClO	15	799	LER, aerosol
08	414	LER, aerosol		PMD band definition v3.1, PMD-p detector	

Table 3: Wavelength information for the PMD bands used in the PMD-based surface LER algorithm. The wavelength definition follows PMD band definition v3.1, so the information applies to MetOp-A PMD data from after 11 March 2008 as well as to all MetOp-B PMD data.
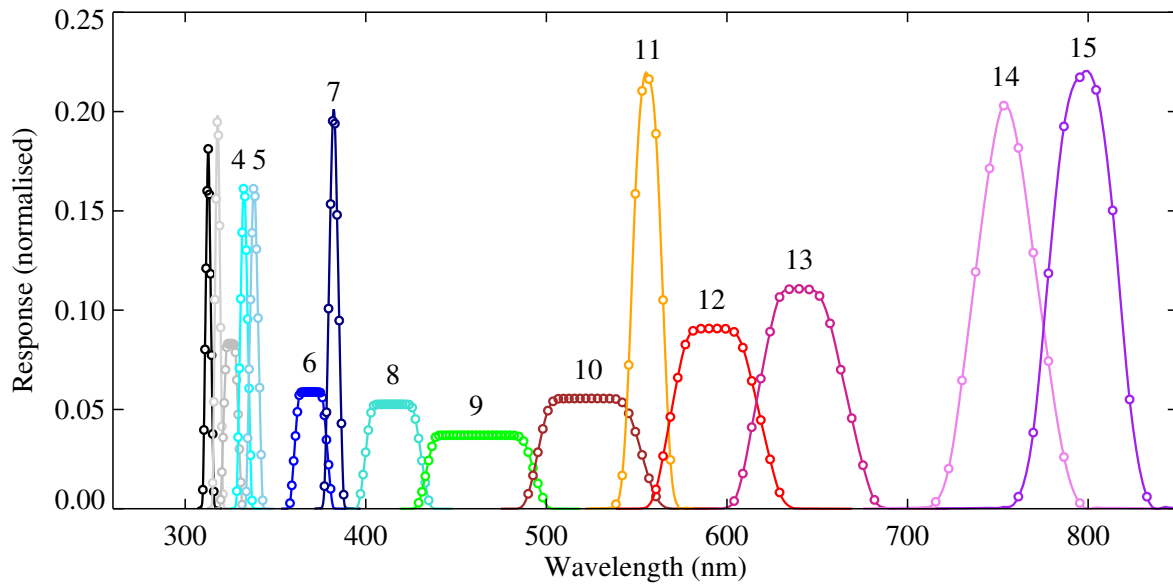
Figure 1: Spectral response functions of the fifteen GOME-2 PMD bands, determined using the slit functions of the underlying detector pixels of the PMD band. Only PMD bands 4–15 are labelled.

For some of the PMD bands the relatively broad wavelength range covered leads to inference with absorption bands. For instance, PMD 14 overlaps with the oxygen-A absorption band and this affects the retrieved surface LER. Likewise, PMD 15 is affected somewhat by water vapour absorption.

3　The basic surface LER algorithm

3.1　Scene LER retrieval

In the algorithm, we start by calculating the values of the surface albedos that are needed to match simulated reflectances to the measured Earth reflectances. These surface albedos are in fact scene albedos, because they include the effects of surface, clouds, and aerosols. The necessary simulations assume a Rayleigh scattering atmosphere which is bounded below by a Lambertian surface. The contribution of the surface to the top-of-atmosphere (TOA) reflectance may be separated from that of the atmosphere according to the following formula [*Chandrasekhar*, 1960]:

$$R(\mu, \mu_0, \phi - \phi_0, A_{\rm s}) = R^0(\mu, \mu_0, \phi - \phi_0) + \frac{A_{\rm s}\, T(\mu, \mu_0)}{1 - A_{\rm s} s^\star} \tag{1}$$

In this equation, the first term R^0 is the path reflectance, which is the atmospheric contribution to the reflectance. The second term is the contribution of the surface with an albedo $A_{\rm s}$. The parameter T is the total atmospheric transmission for the given zenith angles, $s^\star$ is the spherical albedo of the atmosphere for illumination from below, μ is the cosine of the viewing zenith angle θ, and likewise, μ_0 is the cosine of the solar zenith angle θ_0. Using equation (1) and by demanding that the simulated Rayleigh reflectance R_λ equals the measured reflectance $R_\lambda^{\rm obs}$, we find the following expression for the surface albedo $A_{\rm s}$, which is a scene albedo, or more specifically, the scene LER $A_{\rm s}$:

$$A_{\rm s} = \frac{R_\lambda^{\rm obs} - R_\lambda^0}{T_\lambda(\mu, \mu_0) + s_\lambda^\star (R_\lambda^{\rm obs} - R_\lambda^0)} \tag{2}$$

In this equation, R_λ^0 denotes the simulated (path) reflectance at wavelength λ, calculated for the actual atmospheric situation, but without the surface reflection contribution. The path reflectance R^0 can be expanded in a Fourier series. In our case, with a simple Rayleigh atmosphere, this expansion is exact with only three terms in the azimuth angle difference $\phi - \phi_0$:

$$R^0 = a_0 + 2a_1 \cos(\phi - \phi_0) + 2a_2 \cos 2(\phi - \phi_0) \tag{3}$$

The idea of the algorithm setup is that with look-up tables (LUTs) of a_0, a_1, a_2, T, and $s^\star$ we can easily calculate R_λ^0 using equation (3) and $A_{\rm s}$ using equation (2). The advantage of the above approach is that both the azimuthal dependence and the dependence on surface albedo are treated analytically, and are therefore not part of the LUTs. Some interpolation over the remaining parameters is necessary. In this case we have to interpolate over μ and μ_0, surface height $h_{\rm s}$, and ozone column Ω.

3.2　Radiative transfer look-up tables (LUTs)

The look-up tables (LUTs) were created using the radiative transfer code DAK, which stands for "Doubling-Adding KNMI" [*de Haan et al.*, 1987; *Stammes*, 2001]. This vector radiative transfer

model (RTM) takes polarisation into account, as well as ozone absorption and Lambertian surface reflection. The simulations basically describe a cloud-free, horizontally homogeneous atmosphere which is bounded below by a Lambertian surface. We used version 3.2.0 of the DAK RTM. This version supports pseudo-spherical treatment of the Earth's atmosphere. Also, absorption by the O_2–O_2 collision complex is included in the radiative transfer calculations of the LUTs.

The calculations at all wavelengths λ were done for three surface albedos $A_t = \{0.0, 0.5, 1.0\}$, for an azimuth difference $\phi - \phi_0 = 0°$, for 42×42 combinations of the zenith angle cosines μ and μ_0, for cloud-free conditions in a standard Mid-Latitude Summer (MLS) atmosphere [*Anderson et al.*, 1986], for 7 ozone column values $\Omega = \{50, 200, 300, 350, 400, 500, 650\}$ DU, and for 10 surface heights h_s ranging from 0 to 9 km in 1 km steps. The variation of the surface height was achieved by removing an appropriate number of layers from the bottom of the model atmosphere. Such a removal of layers affects the ozone columns to a (very small) degree, which was compensated for by scaling the entire ozone profile in such a way that the original ozone column value was reinstated.

The coefficients a_0, a_1, and a_2, as defined in equation (3), were delivered directly by the DAK code from the runs with albedo $A_t = 0$. The parameters T and $s^\star$ were calculated from the reflectances $R_\lambda(\mu, \mu_0, A_t)$, calculated for the three surface albedos A_t mentioned before, in combination with equation (1). This gives, after some algebra, the following outcome:

$$s_\lambda^\star = \frac{R_\lambda(\mu, \mu_0, 1.0) - 2R_\lambda(\mu, \mu_0, 0.5) + R_\lambda(\mu, \mu_0, 0.0)}{R_\lambda(\mu, \mu_0, 1.0) - R_\lambda(\mu, \mu_0, 0.5)} \ , \tag{4}$$

independent on μ and μ_0, dependent on surface height h_s, ozone column Ω and wavelength λ, and

$$T_\lambda(\mu, \mu_0) = (1 - s_\lambda^\star) \cdot \left(R_\lambda(\mu, \mu_0, 1.0) - R_\lambda(\mu, \mu_0, 0.0) \right) , \tag{5}$$

which is dependent on μ and μ_0, surface height h_s, ozone column Ω, and wavelength λ. The LUTs contain the parameters a_0, a_1, a_2, T, and $s^\star$ for each of the wavelengths. All parameters except $s^\star$ are prepared as a function of μ and μ_0, surface height, and ozone column. The parameter $s^\star$ does not depend on μ and μ_0, and is given as a function of surface height and ozone column.

3.3   From scene LER to surface LER

Most of the scenes for which we calculate the scene albedo contain clouds or aerosols. The retrieved scene LER A_s is therefore usually not representative for the surface LER. In the minimum-LER (MIN-LER) approach followed in *Koelemeijer et al.* [2003] it is acknowledged that scenes can contain clouds, but the presence of (absorbing) aerosols is neglected. In practice, this means one assumes that the lowest value of the scene LER which is recorded for a certain grid cell on the globe over a sufficiently long period of time (say, one month) is most likely a representative cloud-free scene. The scene LER that was retrieved for the respective observation is then taken as the cell's surface LER.

This MIN-LER approach works well for most surfaces, but it can fail for scenes over snow/ice. For such scenes it is hard to distinguish between the albedo of the snow/ice surface and that of overlying clouds. In the paper by *Kleipool et al.* [2008] a new method is introduced which is based on the analysis of the distribution of the scene LER and/or input from external surface (snow/ice) information. In practice, the method distinguishes between two types of approaches. For most situations the 1% cumulative value of the scene LER is used. This is the mean value of the scene LER that is found from averaging the lowest 1% of the collection of scene LERs. This value is usually very close to the MIN-LER result. For snow/ice surfaces, or for surfaces for which the width of the surface LER distribution is small enough (e.g., desert surfaces), the mode of the distribution is taken.

In this algorithm, we follow roughly the same scheme as was introduced by *Kleipool et al.* [2008]. The flowchart of the process is given in Figure 2. Before describing this flowchart, however, we first explain more about the algorithm setup. The globe is described as a longitude/latitude grid containing cells of 1.0 by 1.0 degree (PMD-LER: 0.5 by 0.5 degree). The GOME-2 measurements are subjected to pre-screening: scenes with high amounts of aerosols are filtered out (section 3.5.3) and scenes which were affected by a solar eclipse are also removed (section 3.5.4).

The many remaining GOME-2 footprints are distributed over the longitude/latitude grid, using the centre longitude and latitude to determine in which cell the measurements belong. For each grid cell the observations collected in one month are processed and only the reflectance in a number of wavelength bands is collected (and corrected for the impact of instrument degradation as explained in section 7). For each grid cell the wavelength band at 670 nm is used to select scenes with the correct scene LER (representative for clear-sky conditions) from all the collected scene LERs [*Koelemeijer et al.*, 2003]. So, the flowchart shown in Figure 2 refers to scene LERs retrieved at 670 nm.

The process starts for each grid cell by determining the total number of observations that were collected in the month that is considered. When this number is less than or equal to 5, then the minimum scene LER value is taken as the surface LER value. At the same time, a flag is raised indicating that the result may be suspicious. Usually, this low number of measurements is an indication that the cell was located at or near the edge of the sunlit part of the globe. In other words, the solar zenith angles of the measurements are very high and for part of the month no observations were found.

For other cases the NISE daily snow/ice database [*Nolin et al.*, 1998] is used to determine whether the measured scenes contained permanent ice, sea ice, or snow. The NISE daily snow/ice database is discussed briefly in section 3.5.1. This snow/ice test is only performed for scenes with absolute latitudes above $5°$ because the NISE database is less reliable near the equator. Also, near the equator persistent presence of snow/ice is not expected. When the percentage of measurements that were classified as "permanent ice", "sea ice", or "snow" is above a certain threshold (20%, 1%, and 10%, respectively), then the mode of the scene LER distribution is used to find the grid cell's surface LER value [*Kleipool et al.*, 2008]. For "snow" we also require the mean scene LER to be larger than 0.5.

START

count N, the number of observations in the grid cell for the given
month, collected over all years in the time period

N > 5? — No — MINIMUM
−1
——— take the minimum scene LER ———

Yes

No — LAT > 5°?   (do not use the snow/ice database near the equator)

Yes

ICE
> 20%? — No — SEA ICE
> 1%? — No — SNOW
> 10%? — No

1 Yes   2 Yes   3 Yes

MODE   MODE   MODE

——— take the mode of the scene LER distribution ———

OCEAN? — Yes — 1% CUMULATIVE
255
——— take the 1% cumulative value of the scene LER ———

No

calculate the standard deviation of the scene LER distribution

LAND? — Yes — STDEV
< 0.1? — Yes — MODE
0

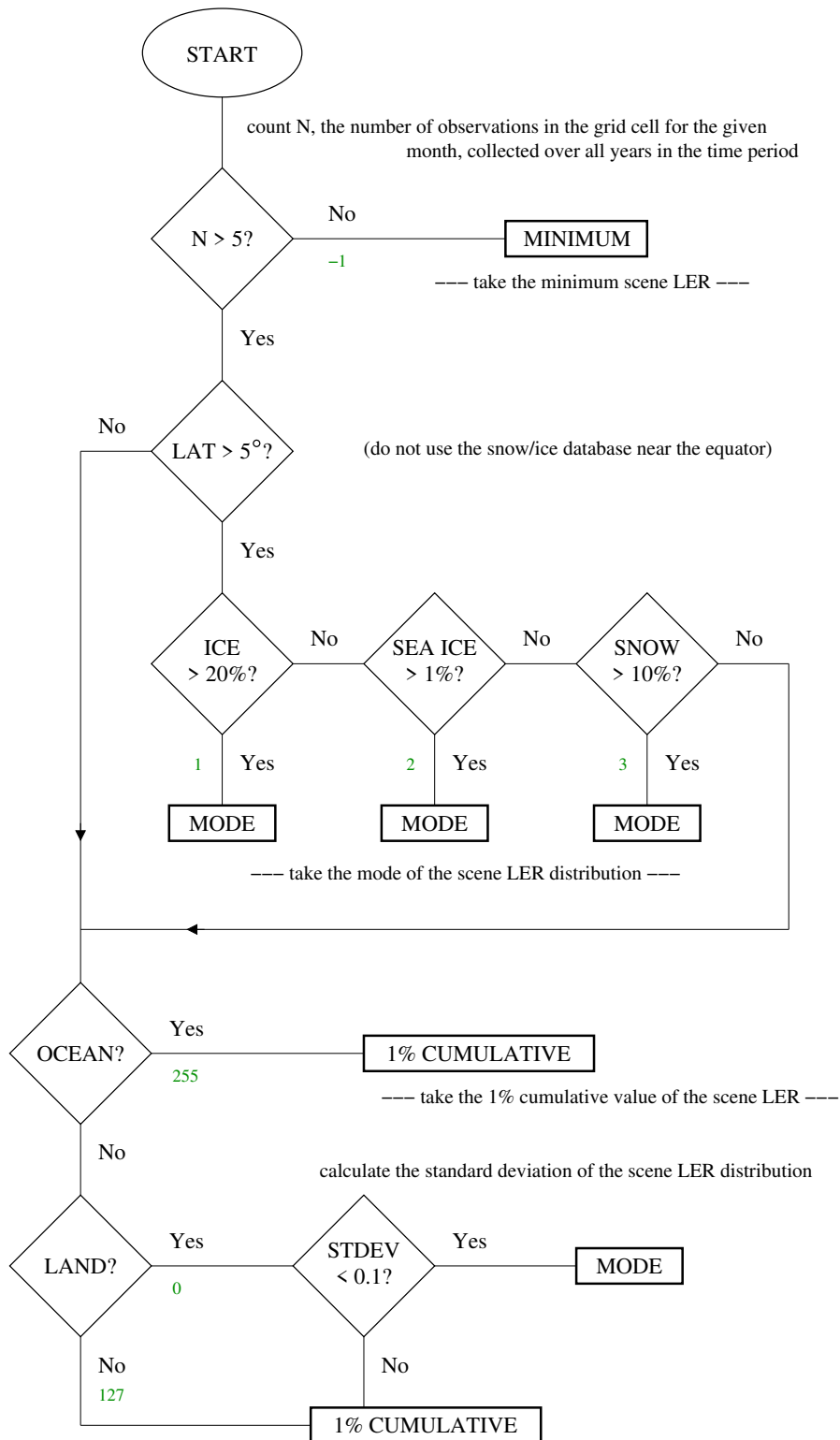No   No
127
1% CUMULATIVE

*Figure 2: Flowchart describing the process of extracting the surface LER for a certain grid cell from
the collected observed scene LER values. More details are provided in the main text.*

For the other (remaining) cases the surface type (land/water) is determined from a GTOPO30 surface type database. This database is discussed in section 3.5.2. When the cell is classified as "water" then the 1% cumulative value is taken for the cell's surface LER. When the cell is classified as "land" then first the standard deviation of the distribution of the scene LER is calculated. If this standard deviation is below 0.1 then the area is considered to be a typical arid desert area and the mode of the scene LER distribution is used to find the grid cell's surface LER value [*Kleipool et al.*, 2008]. If the standard deviation exceeds 0.1 then the 1% cumulative value is taken for the cell's surface LER. If at this point the cell has not been assigned a processing strategy, it is assumed to cover a coastal area and the 1% cumulative value is taken for the cell's surface LER.

In Figure 3 we present, as an example, a global overview of the modes that were used to determine the surface LER for the month May. The data were collected from the years 2007–2013. From the figure it is clear that the desert areas are correctly identified as arid areas. For these scenes the mode LER is used. The minimum-LER approach is used for a small number of measurements. The 1% cumulative value is mostly used. Because of the small number of measurements inside a grid cell (say, 500 measurements for a month of data when 7 years are taken into account), in practice the 1% cumulative value is nearly identical or at least very similar to the minimum-LER value. For that reason, from now on MIN-LER refers to the approach where we use the 1% cumulative value, and MODE-LER refers to the approach where we follow the scheme shown in Figure 2.
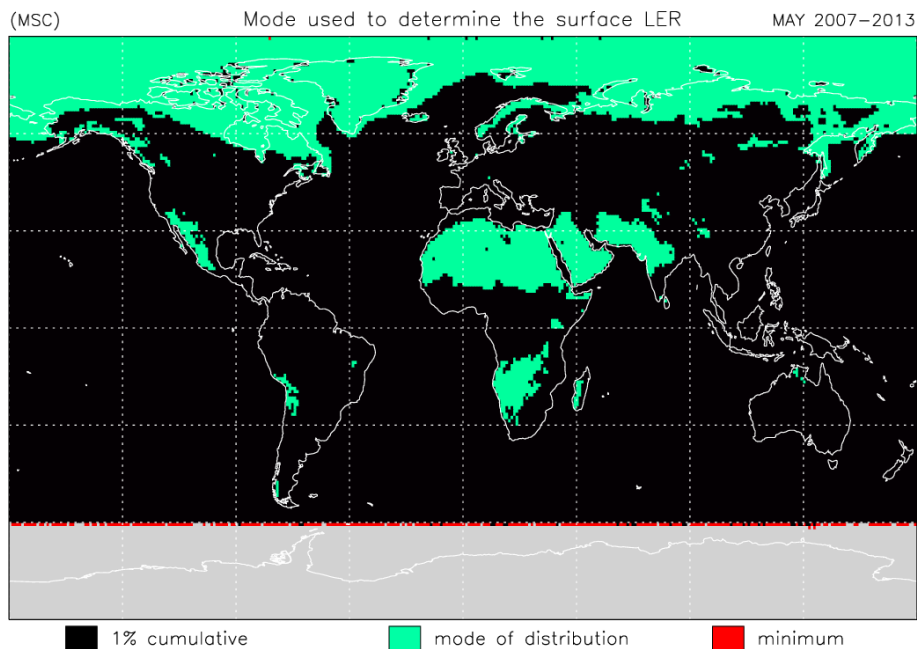

Figure 3: Map indicating where the GOME-2/MetOp-A surface LER algorithm uses the 1% cumulative value (black), the mode of the distribution (green), or the minimum value (red). The data are from the month May. In the grey areas no suitable measurements could be collected ($\theta_0 > 85°$).
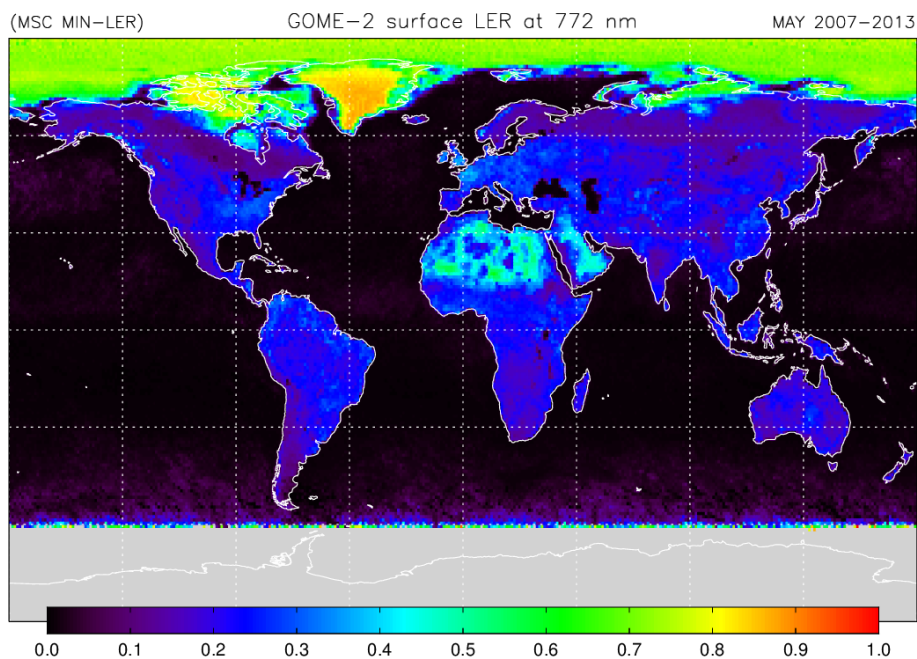
Figure 4: Example of the GOME-2/MetOp-A surface LER for the month May, retrieved for 772 nm using the MIN-LER approach. The data were collected from the years 2007–2013.
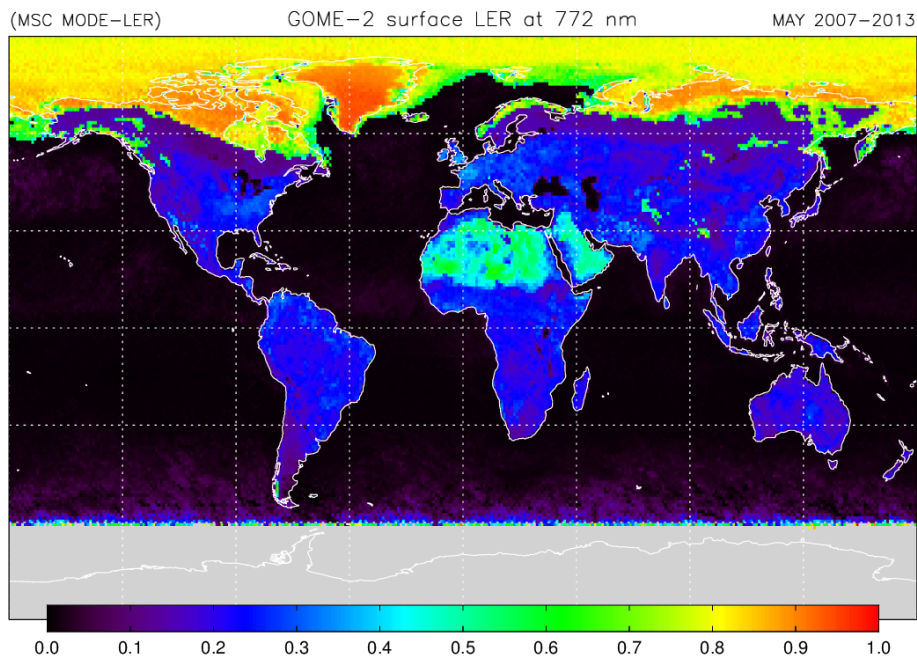

Figure 5: Example of the GOME-2/MetOp-A surface LER for the month May, retrieved for 772 nm using the MODE-LER approach. The data were collected from the years 2007–2013.

As an example of the GOME-2 surface LER product, we present in Figure 4 the surface LER in the month May retrieved from GOME-2 observations at 772 nm. The approach used here was the MIN-LER approach, and the data were taken from the month May of the years 2007–2013. To compare, in Figure 5 the same result is given for the MODE-LER approach. Obviously, there are large differences for the known snow/ice areas and over the arid (desert) areas. The GOME-2 surface LER products will provide both the MIN-LER and the MODE-LER surface LER result.

In this section we presented several images based on data from the GOME-2 instrument on MetOp-A. However, the methods described here apply in exactly the same way to MetOp-B data.

3.4   Essential input parameters for radiative transfer

3.4.1   Ozone

Knowledge of the ozone column associated with the measurement footprint is essential for wavelengths shorter than ∼330 nm or between 450–650 nm. Here ozone absorption has a large impact on the reflectance. We use the GOME-2 level-2 total ozone column product as input for the radiative transfer calculations. Assimilated total ozone columns are available as backup. Please note that at the other wavelengths (including 670 nm) absorption by ozone is of much less importance.

3.4.2   Surface height

The mean surface height for each suitable measurement footprint is determined using a high-resolution surface height database. This surface height database was constructed from an ETOPO-4 elevation database [*National Geophysical Data Center*, 2006], and has an angular resolution of 4 arc-minutes in both latitude and longitude. As we are only interested in the topographic information, all bathymetric information was removed from the database, and replaced by a zero surface height. The mean surface height for each footprint is calculated by first determining the grid points of the surface height database that fall inside the footprint, and then averaging their associated surface heights.

3.4.3   Water vapour

Water vapour information is needed only for the 697 and 712-nm wavelength bands. These two wavelength bands were carefully positioned in the reflectance spectrum, to ensure minimal influence of absorption by trace gases. In spite of this, both wavelength bands are influenced slightly by water vapour absorption. This dependence on the water vapour column is included in the look-up tables. For water vapour column input we make use of a ERA-INTERIM monthly water vapour column

climatology which has a resolution of $0.25° \times 0.25°$. Using a monthly climatology is at this point sufficient, but it is better to make use of real daily water vapour information in the future.

3.5 Input parameters that influence decision-making

3.5.1 Snow, permanent ice, sea ice

To determine whether or not a scene is located over snow/ice surfaces, we make use of the "Near-Real-Time SSM/I-SSMIS EASE-Grid Daily Global Ice Concentration and Snow Extent" product, also known as the "Near-real-time Ice and Snow Extent" (NISE) product [*Nolin et al.*, 1998]. The daily data are used to find for each GOME-2 measurement footprint the snow/ice situation. When the NISE data for a certain day are not available, then the data from the next day are used.

3.5.2 Surface type

The surface type could in principle be deduced directly, at no extra cost, from the NISE data. Additionally, the NISE data also indicate whether or not a pixel covers a coastal area. Nevertheless, it was decided to determine the surface type from a GTOPO30 surface elevation database. The derived surface type indicator can have the value 0 (for "water") or 1 (for "land").

3.5.3 Absorbing Aerosol Index

The Absorbing Aerosol Index (AAI) is calculated within the processing chain. This does not slow down the processing much and has the advantage that there is always absorbing aerosol information available. The algorithm used for the calculation of the AAI is identical to the GOME-2 AAI retrieval algorithm. Details about the GOME-2 AAI retrieval can be found in *Tilstra et al.* [2010].

The AAI is needed to be able to exclude scenes with large concentration of absorbing aerosols. The presence of these aerosols (usually found over cloud-free desert areas in the months June–September) will influence the scene LER and will therefore corrupt the retrieved surface LER. In the code, we filter out all observations for which $AAI > 2$ before analysing the scene LER distribution.

3.5.4 Solar eclipse flag

Solar eclipse events lead to abnormally low values for the retrieved Earth reflectance. Observations taken during a solar eclipse should not be used and the affected measurements need to be removed

from the analysis. For the purpose of doing that, a solar eclipse flag is determined for each observation. The derived solar eclipse flag can have the value 0 ("not affected") or 1 ("affected"). The flag is set according to the information given in Tables 5 and 6 of Appendix B.

3.6   Description of the surface LER data processor

The surface LER data processor was built as a series of steps which deliver intermediate products which are then used by the next step in the process. A graphical representation of the data processor is given in Figure 6. The input consists of GOME-2 level-1b orbits (or PDUs) of version 5.3 and above. The data processor can process level-1b files from the GOME-2A and GOME-2B instruments, without discriminating much between the two. The data from GOME-2A are taken from the period 1 February 2007 to 31 December 2012 (MSC-LER) or from the period 1 April 2008 to 31 December 2012 (PMD-LER). The data from GOME-2B are from the period 1 January 2013 to 30 June 2018.

In the first step of the process the Earth reflectance is calculated for all suitable measurements. Whether or not a measurement is "suitable" is determined by the following check list:

1. Is $\theta_0 < 85°$?

2. Is the integration time (IT) 187.5 ms?   [24 measurements inside each forward scan]

3. Is the measurement from the forward scan?   [backscan measurements are not used]

4. Is the measurement from the descending orbit part?

5. Is the measurement not a PMD RAW mode measurement?

6. Does the Earth reflectance show a physical value?   [sanity checking]

7. Is the measurement not affected by a solar eclipse event?

Check number "7" is coded manually, which is robust and manageable as solar eclipse events are relatively scarce. From the Earth reflectance spectrum the code calculates the mean reflectance for a predefined list of wavelength bands. The following parameters are stored in intermediate files "A":

level1_orbit	the filename of the level-1b orbit
level1_version	the processor version of the level-1b orbit
observation_mode	the measurement mode
narrow_swath	indicator for narrow swath / nadir static mode
$\theta, \theta_0, \phi - \phi_0$	viewing and solar angles

λ	list of selected wavelength bands
channel	spectral channel hosting wavelength band
R_λ	banded Earth reflectances
DateTime	required for finding original observations
centre latitude/longitude	required for gridding and for solving date line problems
corner latitude/longitude	required for e.g. surface height calculation
Index_In_Scan	can be used for e.g. removing scan-angle dependencies
cloud fraction	can be used for e.g. pre-filtering
cloud pressure/height	for distinction between snow/ice and clouds – not used
cloud albedo	not used

These parameters are determined for each PDU or orbit of a certain day, and stored into a file which is placed into a directory structure YYYY/MM/DD. This level-1 extraction is very time consuming and therefore this step of the process does not perform any retrieval steps that might change in the future as the algorithm evolves. The amount of data generated this way amounts to 1.2 Gb per month per year. This completes the description of step "1" of the surface LER data processor.

In step "2" we gather scene information: surface height and type, ozone column, snow/ice information, and AAI (all explained in section 3.4). In step "3" we apply a correction for instrument degradation (explained in section 7) and determine the scene LER using the theory in section 3.1. Steps "2" and "3" are both executed by the same computer code, which at the end produces intermediate products "B" (in HDF-5 format) containing also the additional parameters.

Step "4" focuses on one wavelength: 670 nm. The scene LER at this wavelength is used to determine which scenes are considered representative for cloud-free situations for which the scene LER corresponds to the surface LER. For each grid cell the code stores the date and time of the representative measurements. See section 3.3. Narrow swath observations are skipped in this step.

In step "5" the code uses the DateTime to calculate the surface LER for all wavelengths. This is done by accessing the intermediate HDF-5 files that were produced in step "3" and averaging the scene LER values of the respective wavelength band. Step "4" and "5" are combined into one computer code. The result is an intermediate file which contains the surface LER grid for all wavelengths for the given month, but also other relevant parameters such as the mode that was used, the number of observations per grid cell, the NISE grid, the estimated errors, et cetera.

The surface LER grids in these intermediate files are not ready to be used. First, some of the grid cells over the ocean need to be corrected for what we call cloud contamination. This phenomenon, caused by persistent cloud presence, is explained more clearly in section 4.2. The actual correction for cloud contamination over the oceans is performed in step "6" of the data processor. Note that the surface LER grids inside the intermediate files are only filled for the sunlit part of the globe (for which
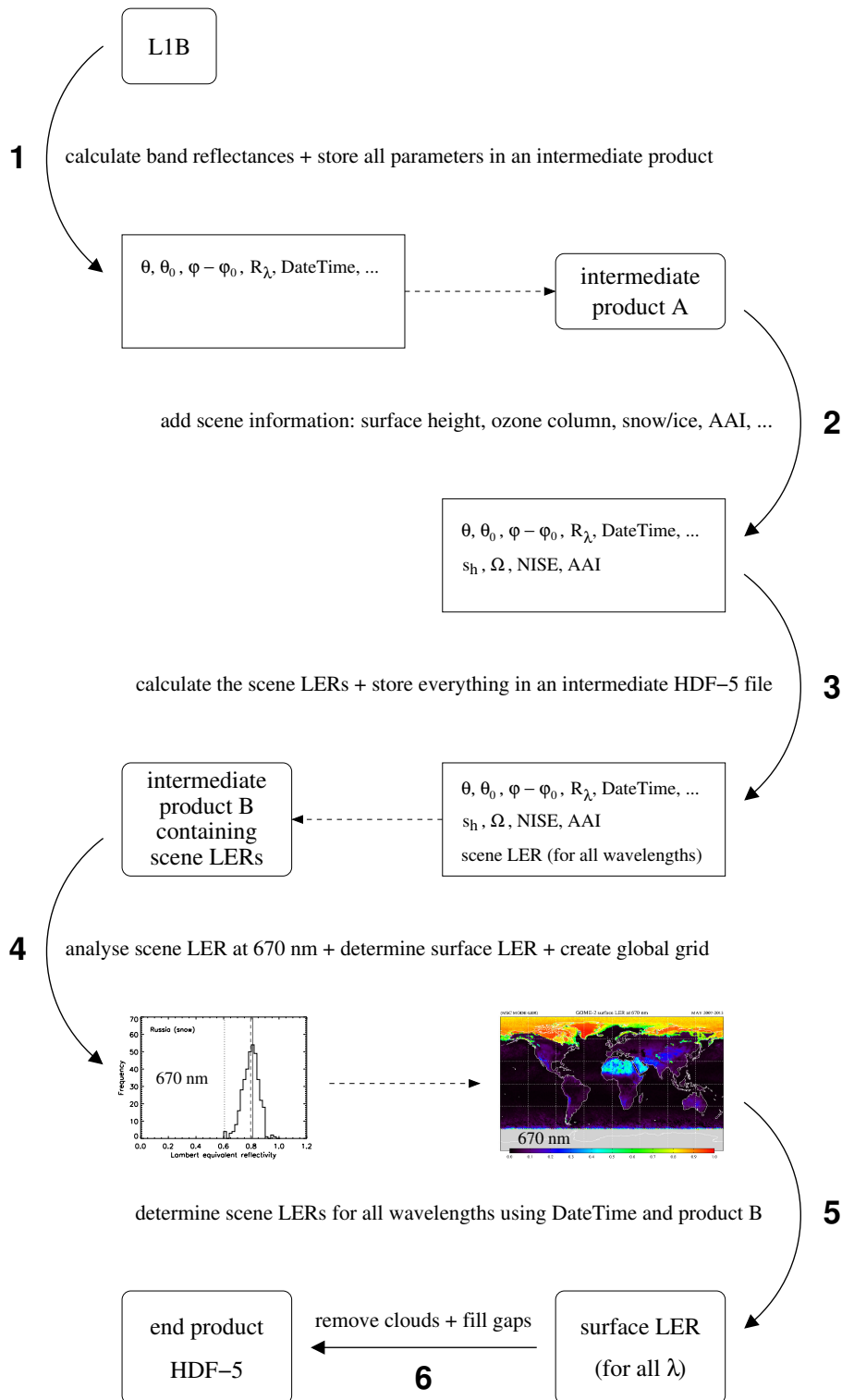
L1B

1 calculate band reflectances + store all parameters in an intermediate product

$\theta, \theta_0, \varphi - \varphi_0, R_\lambda$, DateTime, ...   intermediate product A

add scene information: surface height, ozone column, snow/ice, AAI, ...   **2**

$\theta, \theta_0, \varphi - \varphi_0, R_\lambda$, DateTime, ...
s_h, Ω, NISE, AAI

calculate the scene LERs + store everything in an intermediate HDF–5 file   **3**

intermediate product B containing scene LERs $\theta, \theta_0, \varphi - \varphi_0, R_\lambda$, DateTime, ...
s_h, Ω, NISE, AAI
scene LER (for all wavelengths)

4 analyse scene LER at 670 nm + determine surface LER + create global grid

Russia (snow)
670 nm

670 nm

determine scene LERs for all wavelengths using DateTime and product B   **5**

end product HDF–5   remove clouds + fill gaps   surface LER (for all λ)
6

Figure 6: Schematic overview of the six steps that make up the GOME-2 surface LER data processor.

$\theta_0 < 85°$, see Figure 3). To offer the users of the GOME-2 surface LER product also meaningful data for these missing parts of the globe, grid cells with no data are filled with surface LER values from other months for which the grid cell did contain a trustworthy value. The exact approach followed is discussed in section 4.3. This correction is also performed in step "6" of the data processor.

This last step in the process not only corrects for cloud contamination and handles missing data, but also provides a quality flag and combines the result for the individual months into one HDF-5 file. The data processor operates in exactly the same way for MetOp-A and MetOp-B data. This completes the description of the GOME-2 surface LER data processor.

4 Post-processing corrections and flags

4.1 Introduction

The basic surface LER algorithm was described extensively in section 3. The level-3 products that are created by the data processor are "raw" surface LER products, meaning that they are not yet finished, for a variety of reasons. First of all, for users of the databases the surface LER fields from the twelve individual months of the year need to be combined into one product. Secondly, residual cloud contamination over the oceans is an issue which requires both detection and correction. Thirdly, missing data (mostly due to polar night) needs to be filled in. And finally, flags need to be added to the product to provide information about the reliability and processing history of the data.

4.2 Cloud contamination for cells over the ocean

For grid cells located over the oceans, the data processor is constantly looking for cloud-free scenes from which to determine the surface LER. Sometimes, for certain grid cells, and despite having more than six years of data available, a cloud-free scene is never observed. This happens for regions which are known to be suffering from persistent clouds. Figure 7a presents the minimum FRESCO cloud fraction for each grid cells on the world map. As can be seen, the minimum cloud fraction is close to zero for most of the cells, but for some of the cells, this zero value is not reached. For these cells, the retrieved surface LER is contaminated by the influence of clouds. A correction is needed.

In the data processor, we correct for this effect by looking for donor cells which were not cloud contaminated. The process starts with identifying the contaminated cells. This was initially done by looking at the minimum cloud fraction. However, this approach was abandoned because the (FRESCO) cloud fraction used here uses the GOME-1 surface LER database. This is not an independent source, and it is also suffering from cloud contamination. Also, for the PMD measurements no cloud fraction information is currently available. Note that the need for this correction is somewhat smaller for the PMD-LER because of the smaller footprint size of the PMD measurements.

In step "6" of the data processor, we use the retrieved 772-nm surface LER (PMD-LER: PMD 15) in combination with a threshold to find the cloud contaminated grid cells (over the ocean). This seems to work better than using the cloud fraction. The correction is performed for each of the contaminated cells by finding a donor cell in the vicinity of the contaminated cell. This donor cell is searched in a box around the contaminated cell with dimensions of $10°$ latitude and $30°$ longitude. However, for contaminated cells in the region near the equator where the absolute latitude is less than $30°$, the longitude range of the box is extended to $60°$. The donor cell is the cell in the box with the lowest retrieved 772-nm surface LER. The effect of the correction is demonstrated by Figure 7c.
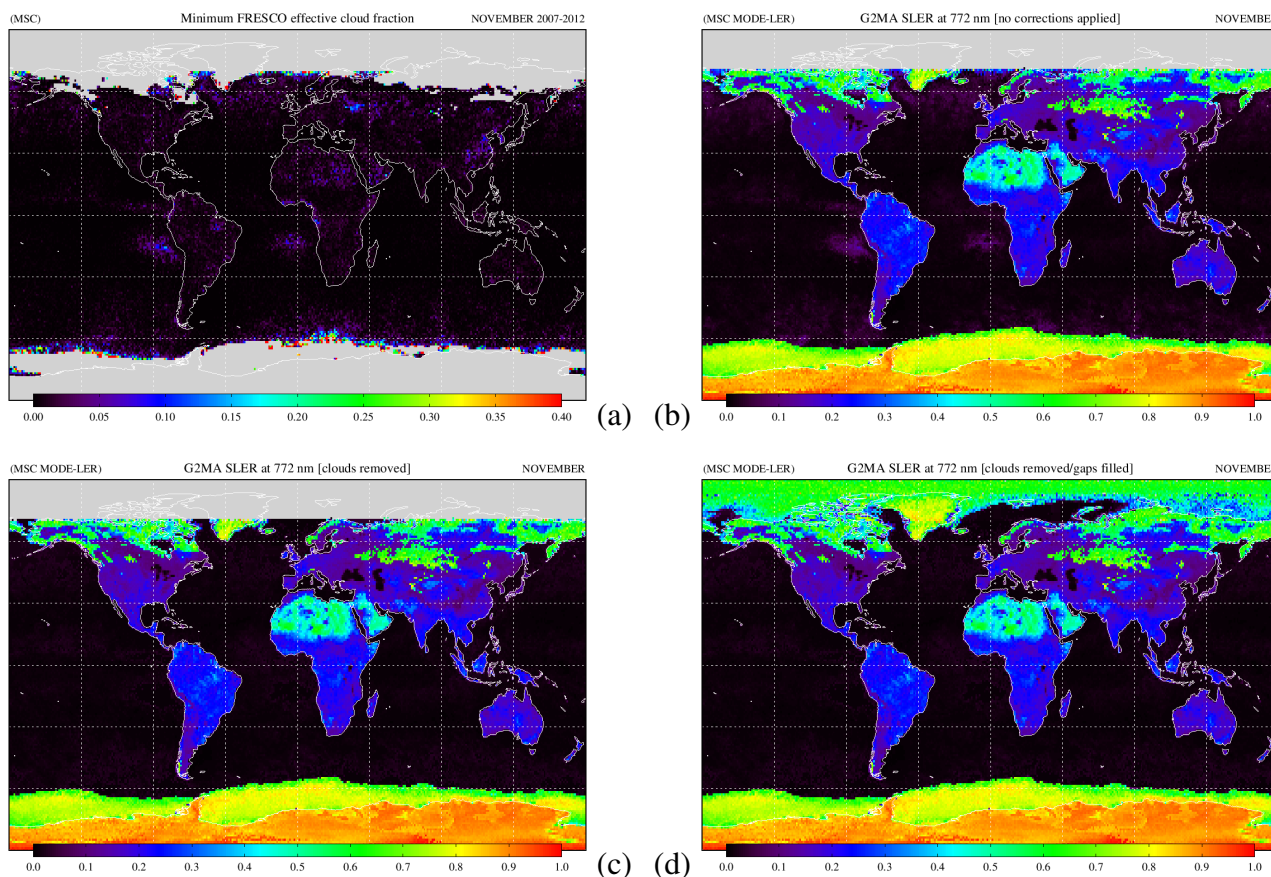
Figure 7: Some intermediate processing results for the month November, determined from GOME-2A observations over the years 2007–2012. (a) Minimum effective FRESCO cloud fraction encountered. (b) Surface LER map showing residual cloud structures over the oceans. (c) Surface LER map after performing the correction for persistent clouds over the oceans. (d) Surface LER map after filling the gaps near the polar regions (due to polar night) with data from other months.

4.3   Filling missing data

Missing data only occurs for grid cells near the polar regions for which the GOME-2 observations (with $\theta_0 > 85°$) were deliberately filtered out. Although the demand for a surface LER value for these geometries seems to be small, some meaningful value should be provided to the users of the data. For that reason, we look for the closest month which does have reliable data for the grid cell in question. We record the surface LER from this donor cell but also its NISE characterisation. We compare the NISE characterisation of the empty cell with the NISE characterisation of the donor cell. When they are identical, then we adopt the surface LER value. When they are not identical, then we jump to the next month which does have reliable data for the grid cell in question and try again. The filling of missing data in step "6" of the data processor is demonstrated in Figure 7d.

Flag	Meaning of flag
0	data are ok; no corrections applied
1	residual cloud contamination above ocean detected – replaced by nearby cloud-free cell
2	residual cloud contamination above ocean detected – no suitable replacement could be found (the pixel remains cloud contaminated and/or receives the LER spectrum of a less than optimal donor cell)
3	missing data for polar regions which are observed only part of the year – filled in using nearest month with reliable surface LER data
4	missing data throughout the entire year
5	suspect surface LER value retrieved for at least one of the wavelengths

Table 4: Definition of the quality flags that are provided along with the surface LER products.

4.4   Quality flags

The quality flags of the surface LER grids are determined mainly by the two correction methods described in this section. The meaning of the flags is given in Table 4. The definition of the quality flag was taken over directly from the paper by *Koelemeijer et al.* [2003]. Normal, non-corrected grid cells have their flag set to zero. The surface LER data for these cells are expected to be highly reliable. For grid cells above sea, the flag may be set to 1 or 2. When the flag is set to 1, this means that the grid cell was classified as cloud contaminated. The surface LER is the surface LER of a nearby donor cell. The surface LER may still be used as it is expected to be reliable. When the flag is set to 2, a replacement could not be found, or the replacement itself was not representative. In this case, the surface LER may still be used but it is expected to be less good.

When the flag is set to 3, the grid cell was not part of the sunlit portion of the Earth for the entire month. Or, more specifically, the number of measurements in the grid cell was below 7 (PMD-LER: below 14). In this case, the data processor looks for replacements in neighbouring months.

The flag is set to 4 when no replacement could be found in the entire year. However, this does not happen very often in practice. The flag is set to 5 when the retrieved surface LER for at least one of the wavelengths larger than 330 nm (PMD-LER: PMDs 4–15) is suspect. This may be because the surface LER value found was negative, or because it was found to be larger than what may be expected from a surface LER value. This happens mostly near the polar regions.

5   Increasing the spatial resolution / dynamic gridding

5.1   Introduction

The previous sections have introduced the methods that are used to derive the surface LER databases at the standard grid size. The size of the grid cells in this standard situation is $1° \times 1°$ for the MSC-LER and $0.5° \times 0.5°$ for the PMD-LER. Increasing the spatial resolution by decreasing the size of the grid cells is possible and easily done, but results in less measurements per grid cell and therefore leads to a lower quality, mostly due to residual cloud contamination by persistent clouds.

For most practical purposes the standard resolution is more than sufficient, but for the retrieval of scenes covering coastlines, scenes containing snow on mountains, or other scenes containing large gradients in surface reflectivity, the standard spatial resolution may actually be insufficient. For this reason, we increase the spatial resolution locally for such cases. This "dynamic gridding" method is explained in section 5.2 (for coastlines) and in section 5.3 (for local land scenes). The dynamic gridding method is followed by a smoothing/interpolation step explained in section 5.4.

5.2   Approach for coastlines

Coastline detection for the database grids at their specific resolution is performed based on the Global Self-consistent, Hierarchical, High-resolution Geography (GSHHG) database [*Wessel and Smith*, 1996]. The GSHHG database offers coastline information for the continents, islands, lakes, rivers, river-lakes, island-in-lakes, and even on the "pond-in-island-in-lake" level. We make use of the highest resolution available of the database, which is the "full resolution" version, available at https://www.soest.hawaii.edu/pwessel/gshhg/. For each of the grid cells in the surface LER grids we can determine whether or not a coastline is contained in the grid cell. For Antarctica we only consider the grounding coastline as a coastline. We do not take rivers and canals into account as these have negligible surface areas. We do take the so-called river-lakes into account. Islands with an area of less than 5000 km are not taken into account, nor coastlines from a "pond-in-island-in-lake".

For the MSC-LER, we start out with the standard grid size, labelled 100×100, and produce in almost the same way surface LER grids based on $0.5° \times 0.5°$ and $0.25° \times 0.25°$ grid cells. These databases are labelled 050×050 and 025×025, respectively. We then take the 025×025 surface LER grid as a basis. We perform a loop over all the 050×050 grid cells, and whenever the 050×050 grid cell contains a coastline, we do not touch the surface LER values of the four associated 025×025 grid cells. However, when the grid cell does not contain a coastline, we overwrite the four associated 025×025 grid cells with the surface LER value of the 050×050 grid cell. We do the same for all other parameters and fields that make up the surface LER product (flags, accuracy fields, et cetera).

Then, in the next step, we loop over the 100×100 grid cells, and whenever the 100×100 grid cell does not contain a coastline, we fill the associated sixteen 025×025 grid cells with the surface LER value of the 100×100 grid cell. The result is a database that has an intrinsic resolution of $1° \times 1°$ for most of the grid cells, but an intrinsic resolution up to $0.25° \times 0.25°$ near the coast.

When producing the 050×050 and 025×025 databases we make sure that the post-processing step that locates empty cells and cells with low number of observations (see section 4.3) only tries to fix the empty cells. This is necessary, because the higher resolution leads to a lower number of observations, and we do not want to search for replacements, as these are not available anyway. We also make sure that in the two steps described above we force the replacement by the lower resolution grid cell in case any of the higher resolution grid cells are flagged as "bad". This happens occasionally.

For the PMD-LER, the approach we follow is very similar. This time we create, next to the database at the standard $0.5° \times 0.5°$ resolution (labelled 050×050), a database with $0.25° \times 0.25°$ resolution (labelled 025×025). We perform the same approach as for the MSC-LER. That is, we start out with the 025×025 grid as a basis. We perform a loop over all the 050×050 grid cells, and whenever the 050×050 grid cell contains a coastline we leave the underlying 025×025 grid cells untouched. If the 050×050 grid cell does not contain a coastline then we overwrite the four associated 025×025 grid cells with the surface LER value of the 050×050 grid cell. We do the same for all other fields.

In Figure 8 we present the MSC-LER MODE-LER field retrieved by GOME-2 on MetOp-AB at 772 nm for western Europe, at the original resolution (left window) and at the increased resolution near the coast (right window). The improvement near the coastline is clear. For non-coastal pixels there are no changes whatsoever. The intrinsic resolution is therefore changing near the coast. The resolution of the grid is $0.25° \times 0.25°$ at all times, for both MSC-LER and PMD-LER.
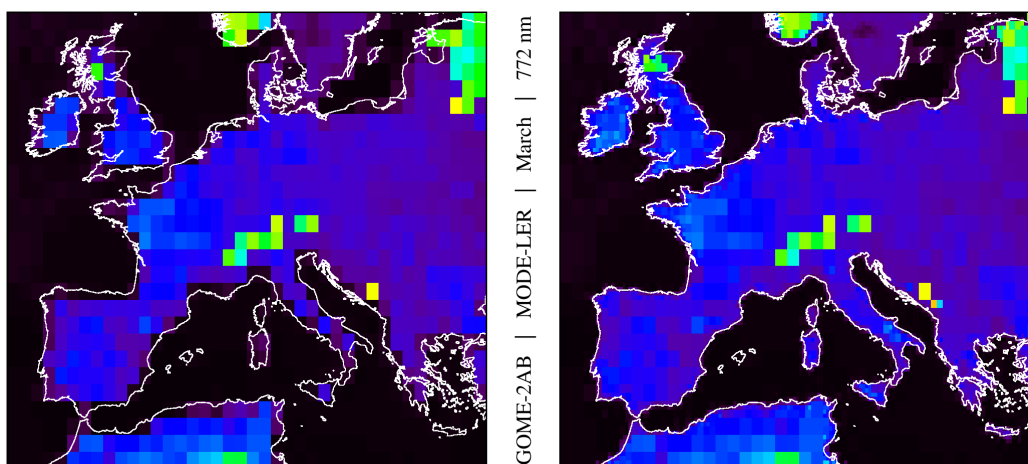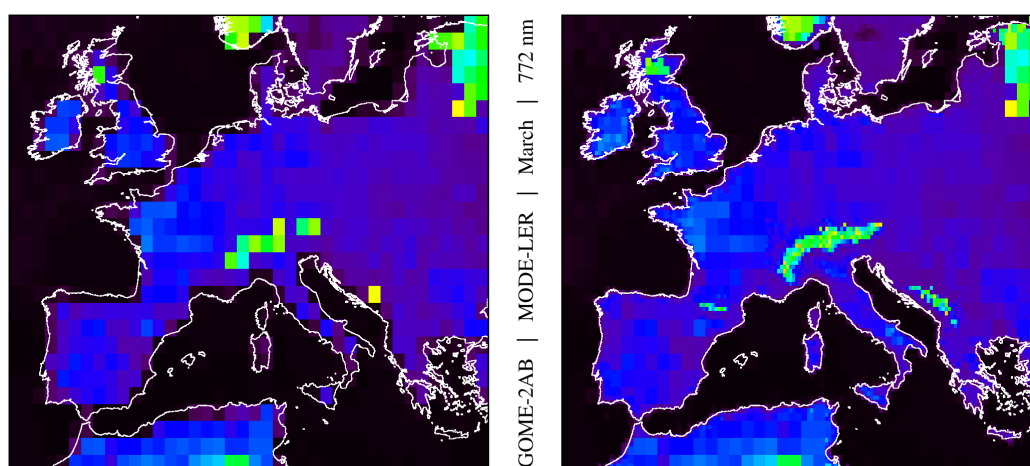

Figure 8: Surface LER retrieved for western Europe at 772 nm (MSC-LER), for the month March. Left: original one-degree resolution; Right: increased resolution of 0.25-degrees near the coast.

5.3 Approach for local land scenes

Over land, large gradients in the surface albedo can exist. For example, permanent snow on mountains will lead to a high contrast with surrounding snow-free areas. A higher spatial resolution is needed to cope with these situations. This is done in a similar way as explained in section 5.2 for coastlines, but now by manually defining regions in which a higher spatial resolution should be used. This can be a resolution of $0.5° \times 0.5°$ or $0.25° \times 0.25°$. In Figure 9 the resulting improvement is shown for western Europe as before in Figure 8. The regions that improved are the ones containing the Alps, the Pyrenees, and the Dinaric Alps, which were given a $0.25° \times 0.25°$ grid resolution.

Figure 9: Surface LER retrieved for western Europe at 772 nm (MSC-LER), for the month March. Left: original one-degree resolution; Right: increased resolution of 0.25-degrees near the coast, as was the case in Figure 8, but now also locally for the Alps, the Pyrenees, and the Dinaric Alps.

For the MSC-LER, these three regions are currently the only regions that receive a higher spatial resolution. For the PMD-LER, the approach is very similar, but next to the Alps, the Pyrenees, and the Dinaric Alps, also the Sahara desert is given the higher resolution of $0.25° \times 0.25°$.

5.4 Interpolation to the high resolution grid

The approach described above leaves us with a database grid of $0.25° \times 0.25°$ resolution that offers a higher resolution near coastlines and for a few regions over land. However, for most of the regions over land and ocean the intrinsic resolution is $1° \times 1°$ and the surface LER grid is filled with redundant information in the form of 4×4 blocks in which 16 identical surface LER values are stored. This is not necessarily a problem, but it does complicate the interpolation that users need to apply to determine the surface albedo for the measurements footprints they are dealing with.

To make things easier for the user the surface LER inside the 4 × 4 blocks is distributed over the 16 grid cells these contain. This is done using standard bilinear interpolation over the 2D surface LER grid. Care is taken to only perform the interpolation inside and between grid cells that have an intrinsic resolution of $1° × 1°$. Other grid cells, such as the ones near the coastline, are left untouched. After the bilinear interpolation a common additive correction factor is applied to the 16 grid cells in such a way that the average surface LER of these 16 grid cells is the same as before applying the bilinear interpolation. This step is needed, because we do not want part of the reflectivity of the surface to disappear from the 4 × 4 blocks as a result of the bilinear interpolation. Next, we repeat the bilinear interpolation and apply the resulting additive correction factor to achieve a slightly higher level of smoothness, making the second 2D field a bit more convincing than the first one.

The result of the interpolation scheme is that the surface LER fields appear to be more smooth. The smoothing that we perform distributes the lower-intrinsic-resolution grid onto the higher-resolution grid. This makes it easier for the user to ingest and use the data without thinking about how to deal with the dynamic gridding that was used. An example of the end result is shown in Figure 10.
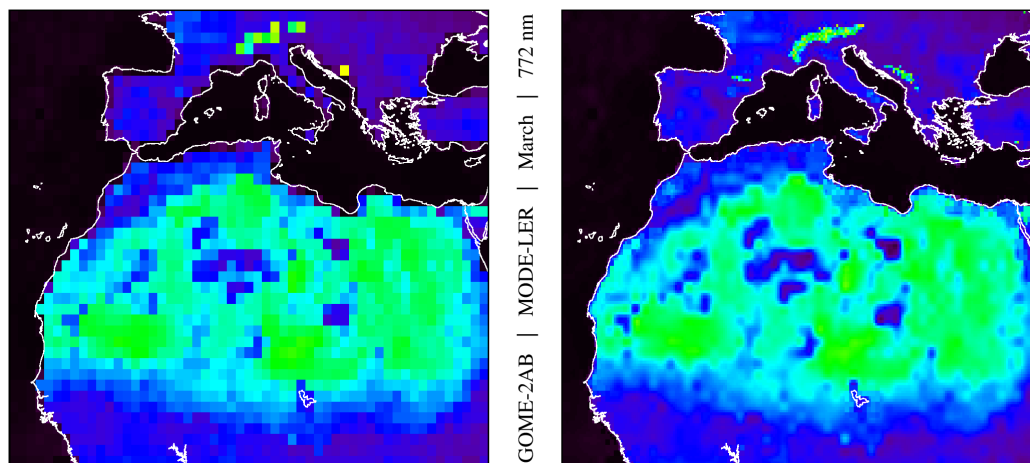
Figure 10: Surface LER retrieved for northern Africa at 772 nm (MSC-LER), for the month March. Left: original one-degree resolution; Right: increased resolution of 0.25-degrees near the coast, for mountain ranges covered by snow, and for all other areas using the interpolation scheme described in the main text. The smoothing/interpolation scheme results in a much smoother surface LER field.

The approach described above is the one that is adopted for the MSC-LER. For the PMD-LER, the approach is similar, except that there are 4 instead of 16 grid cells involved, in 2 × 2 blocks instead of 4 × 4 blocks. Also, for the PMD-LER the bilinear interpolation scheme is only performed inside and between grid cells that have an intrinsic resolution of $0.5° × 0.5°$.

6 Creating a directionally dependent surface LER

6.1 Introduction

This section introduces the concept of a directionally dependent Lambertian-equivalent reflectivity (DLER) to describe surface reflectivity. The surface LER that was defined in the previous sections was based on the assumption that all surface types act as Lambertian reflectors. That is, the amount of light being reflected by the surface is assumed not to depend on the directions of the incoming and reflected light. This principle of Lambertian surface reflection is illustrated in Figure 11a.
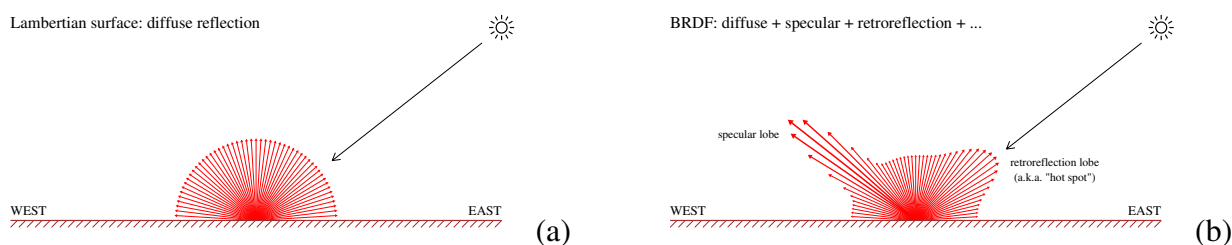
Figure 11: Lambertian surface reflection (a) versus a more realistic situation of surface reflection described by a surface BRDF (b). Unlike the Lambertian model, which does not depend on the exact scattering geometry, the BRDF depends on the directions of the incoming and reflected light.

The assumption of Lambertian surface reflection is, however, not always justified. A more realistic description of the reflective properties of the surface requires a description using a bi-directional reflectance distribution function (BRDF) [*Nicodemus et al.*, 1992] which takes into account the dependence on the incoming and outgoing directions. This situation is illustrated in Figure 11b. The hypothetical surface BRDF contains a specular lobe, resulting from specular reflection by water, and a retroreflection lobe, corresponding to reflection by vegetation in the backscattering direction.

The MetOp satellites were put in Sun-synchronous orbits and the GOME-2 instruments onboard are scanning the Earth's surface looking down. For such geometries, and for a given month of the year, the solar zenith angle (SZA) of an observed location on the Earth's surface should be closely related to the geographical latitude of the location. This is not always the case, for instance, when two neighbouring GOME-2 orbits both observe the same location (at different times and under different viewing and solar conditions). This happens close to the polar regions, where the orbit swaths start to overlap. But, in general, one can say that the SZA dependence is already captured implicitly in the traditional surface LER database. However, the viewing zenith angle (VZA) dependence is not captured at all. This is explained in the next section, which also explains how to proceed.

6.2   Constructing the DLER

The GOME-2 global surface albedo database provides the surface albedo for each geographical location for each of the twelve calendar months. During each such month, a certain geographical location is observed by the GOME-2 instruments from a variety of viewing geometries. In fact, the full range in viewing angles is about 115 degrees. This situation is explained graphically in Figure 12a. The sketched surface BRDF contains a "hot spot" of increased reflectivity near backscattering geometries, which is typical for vegetated surfaces. The reflectivity of the surface is observed by GOME-2 from viewing directions ranging from East to West. Obviously, in an "east" viewing direction the observed surface albedo is lower than in a "west" viewing direction (i.e., near the "hot spot").
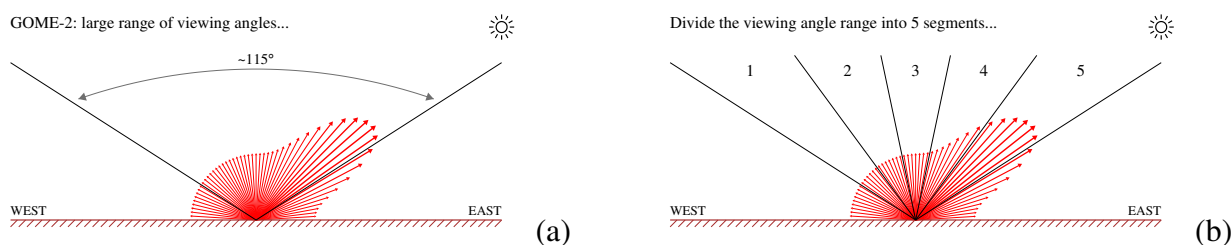
Figure 12: Left: During one month of observations, a certain location is observed many times by GOME-2 for many different viewing geometries (angles). Right: The orbit swath is divided into five viewing ranges and for each segment the surface LER is determined in the usual way.

As explained earlier, in the MIN-LER approach the surface LER retrieval is focusing on the minimum observed scene LER values, so the traditional non-directional surface LER is underestimating the surface albedo at the west side of the orbit swath. For the MODE-LER a similar underestimation occurs. For instruments like GOME-1 and SCIAMACHY, which have narrow orbit swaths, this is not a big problem. For GOME-2, however, this is a serious problem. To address this problem we introduce the concept of a directionally dependent Lambertian-equivalent reflectivity (DLER).

The orbit swath is divided up into five segments, as illustrated in Figure 12b. For each of these orbit swath containers the traditional surface LER is determined, based only on the data that are part of the respective orbit swath segment. This provides us with a surface albedo value for each of the five viewing direction intervals. An example of the retrieved surface albedo is shown in Figure 13.

6.3   Examples of directional dependence

Figures 13 and 14 present examples of the approach that is followed by the new DLER retrieval algorithm. Figure 13 presents the MODE-LER retrieval for a grid cell over the Sahara desert. The
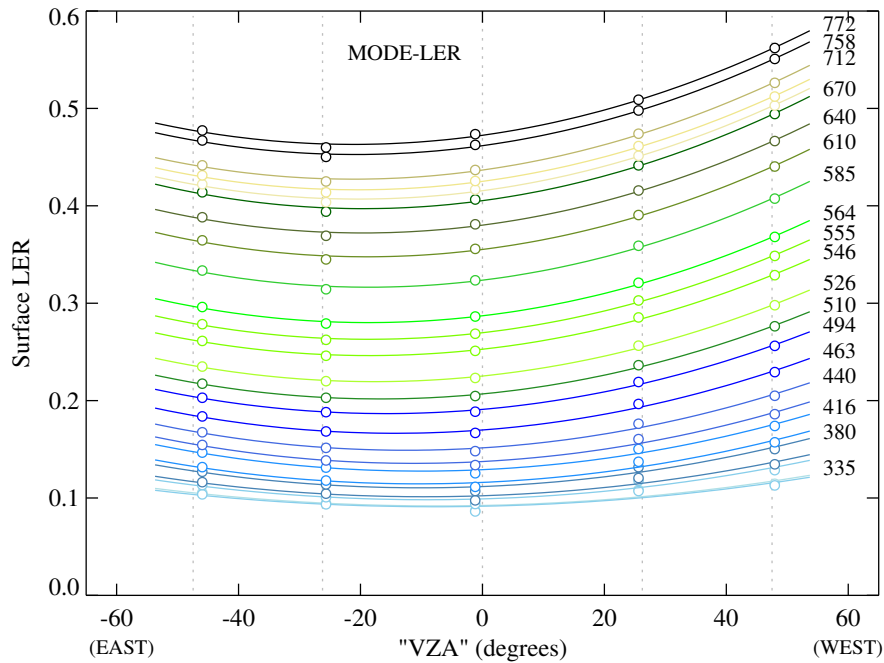
Figure 13: The circles indicate the retrieved (MSC) surface LER for the five orbit swath containers. The associated VZA is plotted on the horizontal axis. Colours indicate wavelength bands. The curves are parabolic fits through the data points. The grid cell is located over the Sahara desert.
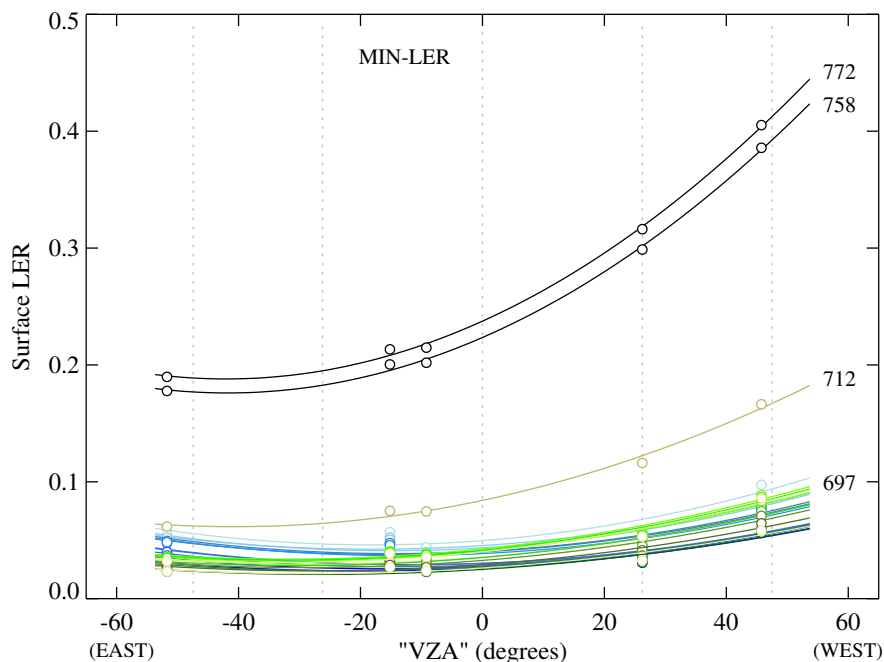

Figure 14: Retrieved (MSC) surface LER for the five viewing angle containers. The associated VZA of the container contents is plotted on the horizontal axis. The grid cell is located over Amazonia.

surface LER was determined in the normal way for the five viewing angle containers. The circles represent the surface LER values (on the vertical axis), for the representative VZA (on the horizontal axis). Both were obtained from the measurements inside the container that were selected to contribute to the surface LER. Different colours are used for different wavelength bands. Note that in Figure 13 the VZA is made negative for observations on the east side of the orbit swath.

There is a clear dependence on the viewing angle, caused by the BRDF effect of the surface. This dependence is important for all wavelength bands. To further analyse the dependence, we perform a simple parabolic fit (as a function of VZA) to the data points. The curves of these fits are shown in Figure 13. As it turns out, for most situations a parabolic fit does a good job describing the VZA dependence. In the fitting process we take into account the errors on the five surface LER values.

Figure 14 presents an example of the MIN-LER retrieval for a grid cell over Amazonia. The surface albedo at 758 and 772 nm is much higher than at the shorter wavelengths, which is typical for vegetated surfaces. For these two wavelengths the surface albedo in the "west" viewing direction is a factor of about two higher than in the "east" viewing direction. But also for the shorter wavelengths there is a significant VZA dependence. This dependence cannot simply be neglected.

6.4   Parameterisation

The coefficients a_0, a_1, and a_2 of the parabolic fit shown in Figures 13 and 14 immediately parameterise the surface DLER for any VZA in the normal range of the GOME-2 instrument. However, in the data product the DLER is presented as a correction on top of the traditional non-directional surface LER field. This has many advantages. Firstly, when the DLER cannot be retrieved by the DLER algorithm it is easy to revert back to the non-directional field. Secondly, the higher spatial resolution near the coastlines (see section 5) needs no additional attention. Thirdly, the user immediately knows from the correction whether or not the surface DLER is really different than the non-directional surface LER, i.e., an additional flag providing this information is not required. Fourthly, the user can at any time switch to the non-directional version by simply setting the correction to zero.

The surface DLER is in the data product is, therefore, expected to be parameterised as a function of the VZA (denoted as θ) in the following way:

$$A_{\mathrm{DLER}} = A_{\mathrm{LER}} + c_0 + c_1 \cdot \theta + c_2 \cdot \theta^2 \,, \tag{6}$$

where θ is negative on the east side of the orbit swath, and positive on the west side of the orbit swath. For water bodies the coefficients c_0, c_1, and c_2 are set to zero. They are also set to zero for coastal areas and for areas for which the DLER could not be retrieved. A failure to retrieve the DLER occurs when not all five viewing angle containers are able to yield enough measurements to derive a reliable surface LER value. This happens only near the polar regions, for high solar zenith angles.

For calculating the coefficients c_0, c_1, and c_2 we use the coefficients a_0, a_1, and a_2 of the parabolic fits as shown in Figures 13 and 14. The c_1 and c_2 coefficients are simply equal to a_1 and a_2, respectively, but the c_0 coefficient is defined as $c_0 = a_0 - A_{\mathrm{LER}}$. In other words, the non-directional surface LER is subtracted. This is in line with equation (6). The coefficients c_0, c_1, and c_2 are dependent on latitude, longitude, month, and wavelength band. Separate calculations need to be performed for the MIN-LER and MODE-LER versions and for the MSC-LER and PMD-LER databases.

6.5 Comparison with MODIS BRDF

In Figure 15 we compare the GOME-2 surface DLER product with the established MODIS BRDF product [*Schaaf and Wang*, 2015] for a 1×1 degree latitude/longitude box in the Amazon region. The MODIS kernel coefficients (f_{iso}, f_{vol}, f_{geo}) are taken from the MODIS MCD43C1 product, which has a spatial resolution of 0.05×0.05 degrees. We downloaded the MCD43C1 product for 15 March 2008, so it can be compared to the DLER result of the month March. To simulate the scanning motion of GOME-2, we let the viewing angle run from -55 to +55 degrees, and set realistic SZA and RAA, which both depend on the viewing angle. This is to simulate the fact that east-viewing and west-viewing directions for the same location will in general have been measured at different solar positions. The geometric and volumetric kernels K_{vol} and K_{geo} are calculated from the viewing and solar angles and the BRDF can be calculated from the kernels and the kernel coefficients.
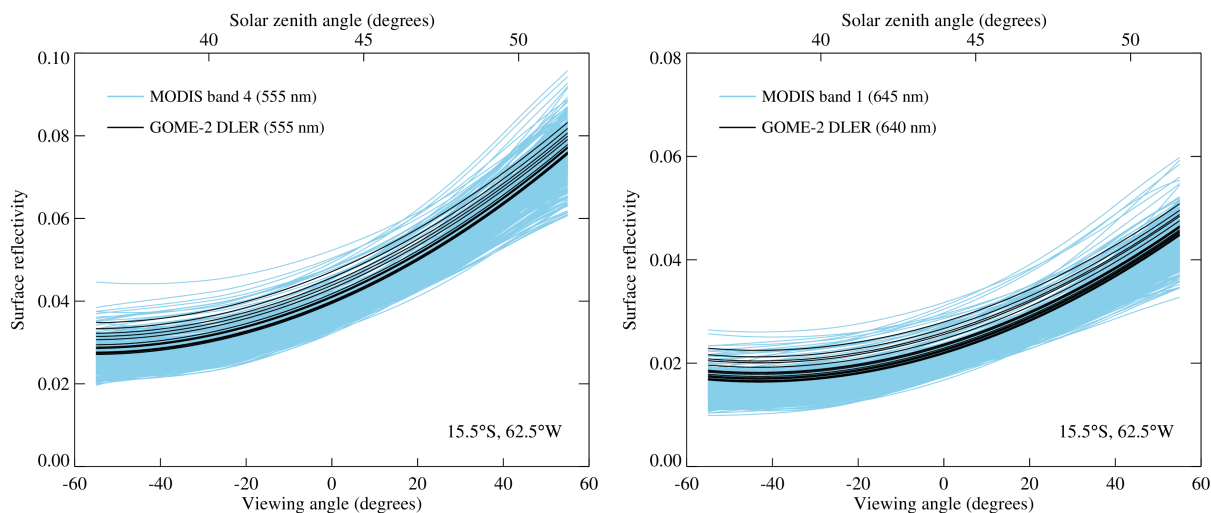

Figure 15: MODIS BRDF versus GOME-2 DLER for a 1×1 degree latitude/longitude box in Amazonia. The scanning motion of GOME-2 is simulated by letting the viewing angle run from -55 (east-viewing) to +55 degrees (west-viewing), with SZA and RAA depending on the viewing angle.

The left window presents the comparison for MODIS band 4, which is centred around 555 nm. This band can be compared well to the 555-nm DLER wavelength band. In the right window MODIS

band 1, centred around 645 nm, is compared to the 640-nm DLER wavelength band. For both wavelengths, there is quite a good agreement between the MODIS BRDF and GOME-2 surface DLER. This is to be expected, because for the wavelengths involved (555 nm and 645 nm) there should not be a large difference between BRDF and surface DLER. This is because the optical thickness of the atmosphere is relatively low at these wavelengths, and light paths involving multiple surface reflections are rare. In any case, the agreement is a strong indication that the GOME-2 surface DLER product is found to exhibit the expected directional behaviour when compared to MODIS BRDF.

The MODIS MCD43C1 data product was retrieved from the online Data Pool, courtesy of the NASA Land Processes Distributed Active Archive Center (LP DAAC), USGS/Earth Resources Observation and Science (EROS) Center, Sioux Falls, South Dakota, https://lpdaac.usgs.gov/data_access/data_pool.

6.6   Summary

The new surface DLER algorithm provides surface BRDF for the GOME-2 instruments, and for instruments from other satellites with a similar overpass time, such as ERS (10:30 LT), Envisat (10:00 LT), and for the future Sentinel-5 mission (09:30 LT). We find good agreement between the GOME-2 surface DLER and the established MODIS BRDF product.

The DLER algorithm only provides surface DLER for areas over land (covered by snow or not), permanent ice, and water covered by sea ice. The algorithm does not try retrieve DLER over water bodies. A first reason for this is that the surface albedo over water depends on parameters which cannot be cast into a climatology that easily, such as wind speed and (to a lesser degree) chlorophyll concentration. Secondly, because of the strong dependence of specular reflection on the viewing and solar angles involved, changes of the solar position during a month influence the albedo much more than for land. Thirdly, the albedo of the ocean can be modelled quite well, taking into account the angular dependence and the dependence on wind speed and chlorophyll concentration.

Therefore, we only provide the DLER above land and sea ice surfaces. For water bodies the traditional non-directional surface LER is provided, which is representative for the diffuse component of the reflection off the water surface. Sun glint is not captured nor contained in the DLER database.

7   Instrument degradation and recalibration

7.1   Introduction

Instrument degradation is a serious problem which strongly affects the Earth reflectance measurements performed by GOME-2 in the UV wavelength range [*Tilstra et al.*, 2012b]. As a result, it also has an impact on the retrieved surface LER values in the UV. The method for in-flight degradation correction that we use has been introduced earlier in *Tilstra et al.* [2012a] for the SCIAMACHY instrument. The method was later applied to the GOME-2 instrument [*Tilstra et al.*, 2012b].

7.2   Analysis

The method is based on studying time series of the daily global mean reflectance. The daily global mean reflectance, denoted by $R^\star$, is defined as the mean of all measured Earth reflectances for a certain scan mirror position on a certain day between 60°N and 60°S and solar zenith angles θ_0 less than 85 degrees. In Figure 16 we present two plots as done in *Tilstra et al.* [2012b] which show the daily global mean reflectance as a function of time for the GOME-2A instrument.

The time series of the global mean reflectance show seasonal variations as well as trends due to instrument degradation. To analyse the time series, we assume that the global mean reflectance may be well described empirically by a function made up of a polynomial term, representing the reflectance change due to instrument degradation, multiplied by a term periodic in time that represents the normal seasonal variation of the global mean reflectance. In other words,

$$R^\star_{\lambda,s} = P^{(p)}_{\lambda,s} \cdot [1 + F^{(q)}_{\lambda,s}] \,, \tag{7}$$

where the term P represents the polynomial part of degree p, defined by

$$P^{(p)}_{\lambda,s}(t) = \sum_{m=0}^{p} u^{(m)}_{\lambda,s} \cdot t^m \,, \tag{8}$$

while the seasonal variation F is described by a finite Fourier series of order q, according to

$$F^{(q)}_{\lambda,s}(t) = \sum_{n=1}^{q} [v^{(n)}_{\lambda,s} \cdot \cos(2\pi n t) + w^{(n)}_{\lambda,s} \cdot \sin(2\pi n t)] \,. \tag{9}$$

In these equations, the parameter t is the time expressed in years since the beginning of the time series (which is 23 January 2007 in the case of GOME-2A and 12 December 2012 in the case of GOME-2B). The parameter λ refers to the wavelength and the integer s relates to the scan mirror position. For GOME-2, this integer runs from 1 to 32 for the nominal integration time (IT) of 187.5 ms

when the instrument scans from east to west and back. Backscan measurements are not considered. Therefore, s effectively runs from 1 to 24. For the present baseline, we use $p = 4$ and $q = 6$.

The polynomial part P is the most important as it represents the relative change in the GOME-2 measured Earth reflectance over the years, per scan mirror position, due to instrument degradation. Normalisation of P immediately leads to the reflectance degradation factor:

$$d_{\lambda,s}(t) = P_{\lambda,s}^{(p)}(t) \, / \, P_{\lambda,s}^{(p)}(0) \, . \tag{10}$$

For GOME-2 the reflectance degradation factor is growing with time for most wavelengths, and is strongly dependent on scan mirror position. Figure 16 shows the behaviour for 328 and 380 nm.
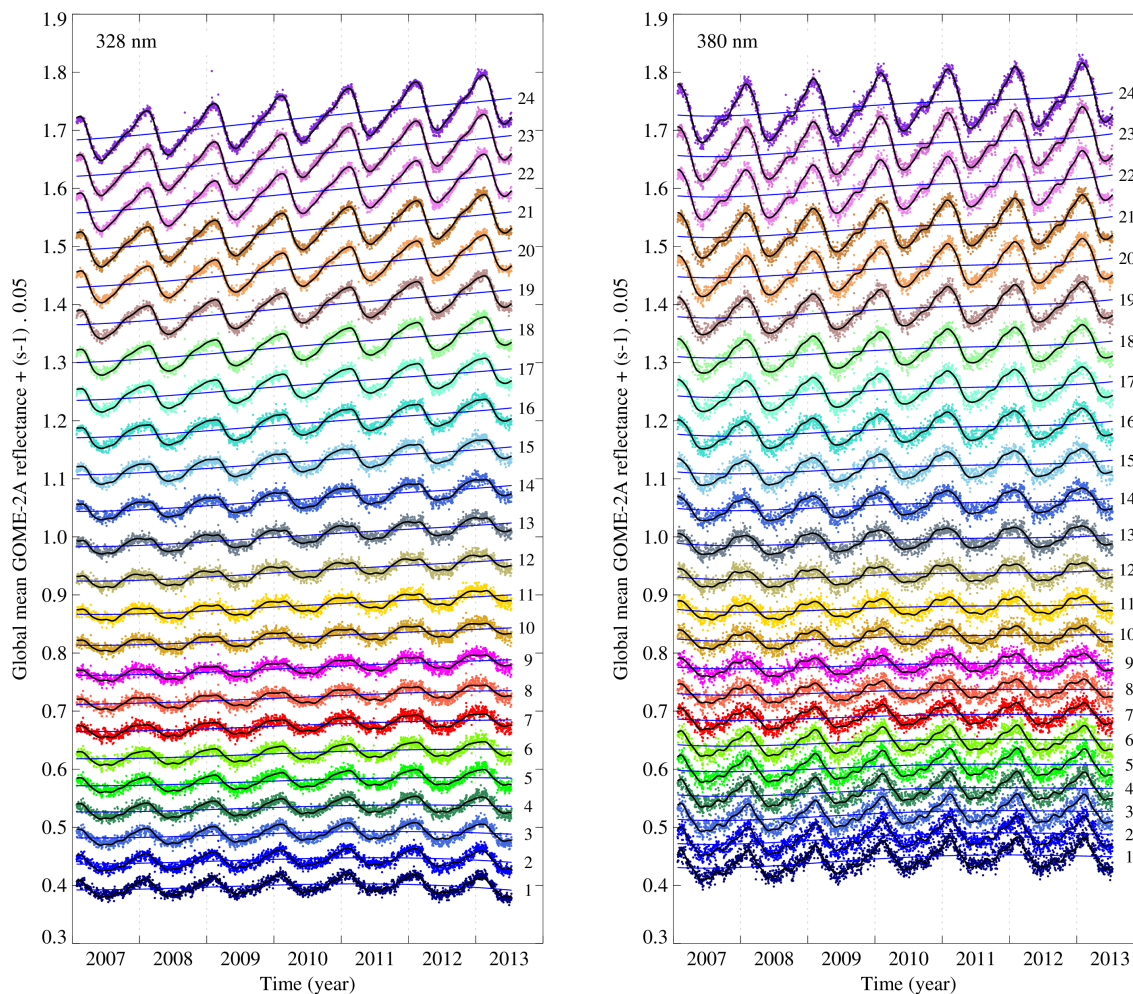
Figure 16: Global mean reflectance measured by GOME-2A at 328 nm (left) and 380 nm (right) as a function of time, for each of the 24 scan mirror positions in the forward scan. To separate the time series graphically, an offset of $(s - 1) \cdot 0.05$ was added to each, where s is the scan mirror position as indicated. The solid black curves are fit results and are described in the main text. The blue monotonous curves illustrate the effect of instrument degradation over the years.

In the current baseline, the time range analysed for GOME-2A is 23 January 2007 to 15 July 2013, which is the time period during which GOME-2A operated in normal swath mode. Analysing measurements after 15 July 2013 is possible but would require adaptations. However, this is not done because the reduced swath data are not used by the data processor any way. The time range analysed for GOME-2B is 12 December 2012 to 30 June 2018. The time ranges provided here do not define the time ranges for the level-1 data that are processed by the GOME-2 surface LER data processor.

7.3   Correction

The correction for instrument degradation can easily be calculated using

$$c_{\lambda,s}(t) \equiv 1/d_{\lambda,s}(t) = P_{\lambda,s}^{(p)}(0) \, / \, P_{\lambda,s}^{(p)}(t) \,. \tag{11}$$

The measured Earth reflectances have to be multiplied with these correction factors. Note that the global mean reflectances can be calculated directly from the intermediate products "A" (or "B") in Figure 6. The correction in equation (11) is applied at the beginning of step "4" in Figure 6.

7.4   Examples

Figure 17 presents, just like Figure 16 did, two plots showing the daily global mean reflectance at 328 and 380 nm as a function of time for the GOME-2A instrument. The difference is that this time the degradation correction factors that were defined in section 7.3 were applied to the reflectances before calculating the global means. As expected, the application of the degradation correction factors has successfully removed all trends that were present in Figure 16.

7.5   Recalibration

Because GOME-2A and GOME-2B data are combined in the retrieval code, it is important that both instruments are well calibrated with respect to each other. If we compare Figure 17, which is based on GOME-2A data, with a similar plot based on GOME-2B data (not shown), then we find that there are only very small differences. In other words, both instruments are well in agreement with each other. However, if we look at the PMD versions of these plots, we find small, but somewhat larger, differences. This can be explained by the start of the time series. The PMD time series of GOME-2A does not not start on 23 January, as the MSC time series does, but on 13 March 2008, right after the PMD band definition change to version 3.1 [*EUMETSAT*, 2015, p. 17]. The degradation correction therefore corrects degradation back to 13 March 2008. It does not correct for degradation all the way
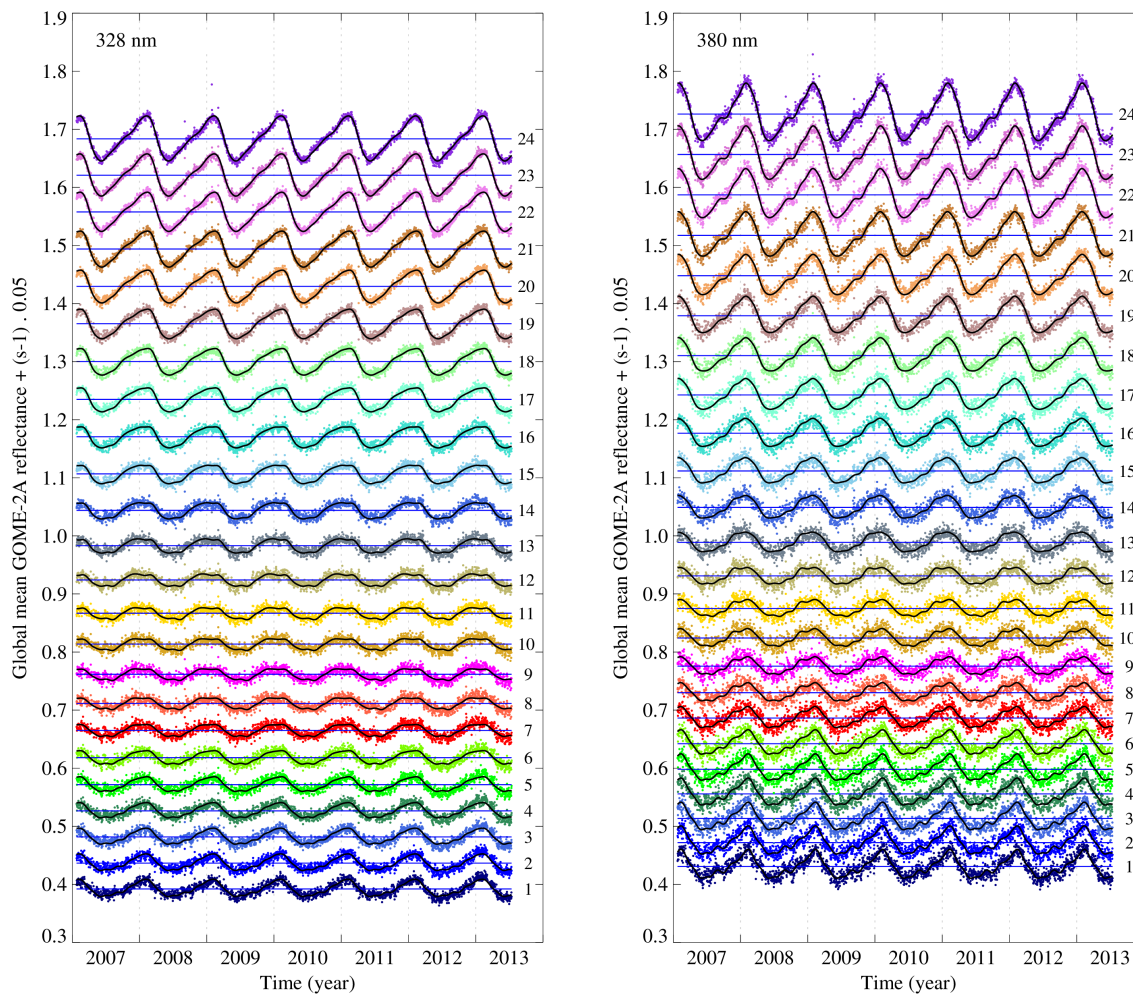
Figure 17: Global mean reflectance measured by GOME-2A at 328 nm (left) and 380 nm (right) as a function of time, for each of the 24 scan mirror positions in the forward scan. The applied degradation correction has removed all trends that are present in Figure 16.

back to 23 January 2007. The PMD reflectance therefore suffers from the degradation that occurred until 13 March 2008. Although the effect is not extremely large, it needs to be corrected.

We therefore assume GOME-2B as the reference instrument, and apply no additional calibration correction to the GOME-2B reflectances. The GOME-2A reflectances are recalibrated. This holds for both the MSC and PMD reflectances. The multiplicative correction factor is a time independent correction factor, but dependent on wavelength band and scan mirror position. It is defined in the following way. We perform the fit function to the degradation corrected time series of global mean reflectance, as shown in Figure 17, for both GOME-2A and GOME-2B. However, for the polynomial part P we now use $p = 0$, so we end up with only one polynomial coefficient, namely $u_{\lambda,s}^{(0)}$. The ratio of the polynomial coefficients $u_{\lambda,s}^{(0)}$ from GOME-2B and GOME-2A is the multiplicative correction factor that we need to apply to the GOME-2A reflectance.

8 Error analysis

8.1 Introduction

The uncertainty on the retrieved surface LER value depends highly on the number of scenes that were selected as representative for a grid cell. If, for instance, the mode of the frequency distribution is selected, there will usually be quite a high number of scenes regarded as representative, and the estimated error on the surface LER will be determined for each wavelength band primarily by the standard deviation in the representative scene LERs. This standard deviation is usually small. If, on the other hand, the 1% cumulative value is used, there are usually much less measurements available and the standard deviation is usually higher. But there are also error sources related to the modelling of the scene and related to errors in the reflectances measured by the GOME-2 instrument.

8.2 Impact of radiometric calibration errors

The sensitivity dA/dR of the retrieved surface LER A to errors in the measured Earth reflectance R can be calculated in a straightforward way from equation (2) by differentiation. This yields

$$\frac{dA}{dR} = \frac{(1 - As^\star)^2}{T} \ . \tag{12}$$

Figure 18 presents a plot of the sensitivity dA/dR as a function of surface LER for a selection of wavelengths ranging from 325 nm to 772 nm. The calculations for this plot were performed using the radiative transfer model DAK, for clear-sky conditions in a standard MLS atmosphere (ozone column 334 DU), for nadir view ($\theta = 0°$) and solar zenith angle $\theta_0 = 60°$.

In the visible wavelength range an error of 0.01 in the reflectance leads to an error of approximately 0.01 in the retrieved surface LER, as expected. In the UV, this error increases enormously due to the smaller contribution of the surface to the TOA reflectance. Below 330 nm, retrieval of the surface LER is challenging (if not impossible) and would require a near perfect radiometric calibration as well as reliable information about the shape of the ozone profile for each of the measurement footprints. This is currently not feasible, but at the same time there is also no existing strong demand from the remote sensing community for surface albedo information below 330 nm.

8.3 Error calculation

Given an absolute error δR in the measured Earth reflectance R we can use equation (12) to determine the contribution of this error to the retrieved scene LER A via $\delta A \approx (dA/dR) \cdot \delta R$. Note that the
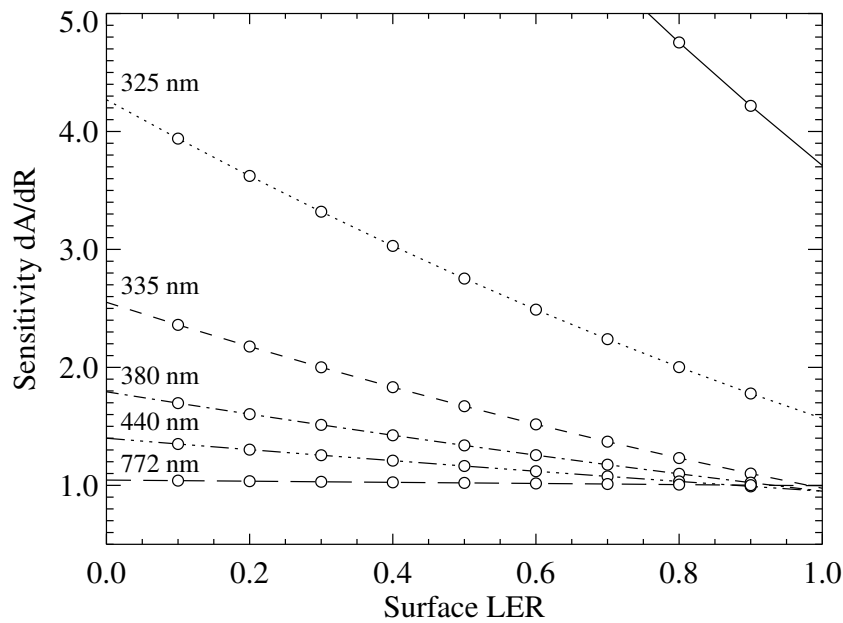
Figure 18: Sensitivity of the surface LER to changes in the Earth reflectance, as a function of surface LER and for different wavelengths. Below 330 nm the sensitivity increases dramatically.

parameters T and $s_\star$ in equation (12) are already known, and that the parameter A is the scene LER itself. The error that is calculated this way is correct for all observations. But, by definition, it is the error on the scene LER, not the error on the surface LER. As such, it does not indicate whether or not the scene LER is representative for the surface LER.

For each surface LER value, the retrieval code will produce two types of errors: (1) a systematic error δA_{sys} based on the systematic error δA, and (2) a statistical error δA_{stat} based on the spread in the observations of the scenes that were selected as so-called representative cloud-free scenes. The systematic error δA_{sys} is calculated as the root-mean-square error (RMSE) of the systematic errors δA calculated for the observations that were selected as representative cloud-free scenes. For the error δR we assume a typical value of 0.01 to be in line with the accuracy of the GOME-2 instruments.

The statistical error δA_{stat} is defined as the standard deviation of the scene LER values of all the selected cloud-free observations. Whether the surface LER was based on the mode of the distribution or on the 1% cumulative value makes in principle no difference. Note that in certain extreme cases the total number of scenes collected N may be lower than 100. In these cases the 1% cumulative surface LER value is determined from only one measurement (from which a standard deviation cannot be determined). Situations like these occur for grid cells which are located near the polar regions (close to polar night), so that only few sunlit observations are collected. Some of these grid cells may have been filled with donor cell information from neighbouring months (see section 4.3).

Note that the general assumption of the retrieval algorithm is that the set of representative cloud-free scenes is well chosen. If the collection contains cloud contaminated scenes, then this will show up as an increase in the statistical error δA_{stat}. Therefore, the statistical error δA_{stat} may be used to estimate the reliability of the surface LER value. In contrast, the systematic error δA_{sys} contains information about uncertainty due to the radiometric calibration but holds no information at all about the reliability of the surface LER value in terms of residual cloud contamination.

9   Proposed validation

Validation of the retrieved GOME-2 surface LER database may be done by comparison with the other surface LER databases that were discussed in section 2. From these, the GOME surface LER database [*Koelemeijer et al.*, 2003] makes most sense as a reference, because of the orbital and instrumental similarities between GOME and GOME-2, and their overlapping set of LER wavelength bands. Note that the GOME surface LER database was essentially retrieved using the MIN-LER approach (as explained in section 3.3), so a comparison with the GOME surface LER will in principle only allow validation of the GOME-2 surface LER determined using the MIN-LER approach.

The OMI surface LER database [*Kleipool et al.*, 2008] may be used for the wavelengths below 500 nm. The OMI surface LER database is important to have as a reference because it makes use of the same surface LER retrieval approach as the one described in this ATBD. That is, both the GOME-2 MIN-LER and MODE-LER surface LER products can be compared and this will provide information on the correctness of the GOME-2 surface LER algorithm (and products).

Alternatively, a comparison with non-LER surface albedos, such as the MERIS black-sky albedo (BSA) [*Popp et al.*, 2011], is also possible. This is strictly speaking not correct, because the BSA is the integral of the bidirectional reflectance distribution function (BRDF) over the entire hemisphere whereas the LER is derived from the much smaller range of viewing angles of the satellite's observation geometry. Also, the LER approach by definition assumes a direction-independent surface albedo. Nevertheless, a comparison would be feasible and worth the effort. Note that a comparison only makes sense over land, because the MERIS surface albedo values over sea are not retrieved from MERIS observations. They were taken directly from the GOME surface LER database.

For the DLER database, which contains the directional dependence of the surface reflectance, the only reference available for validation is the established MODIS BRDF product [*Gao et al.*, 2005; *Schaaf and Wang*, 2015]. However, a comparison between DLER and BRDF is by definition limited in meaning, because the two properties are fundamentally different, by definition. Nevertheless, it may be possible to do the comparisons under certain conditions for which the difference between DLER and BRDF should be small. This is the case for the longer wavelengths.

Validation results are reported in the Validation Report (VR), but also in *Tilstra et al.* [2017].
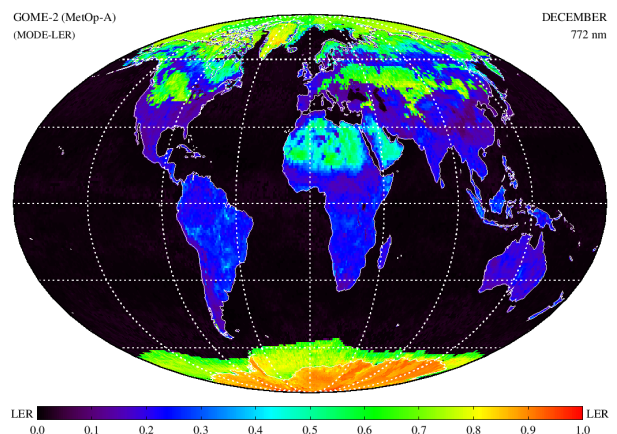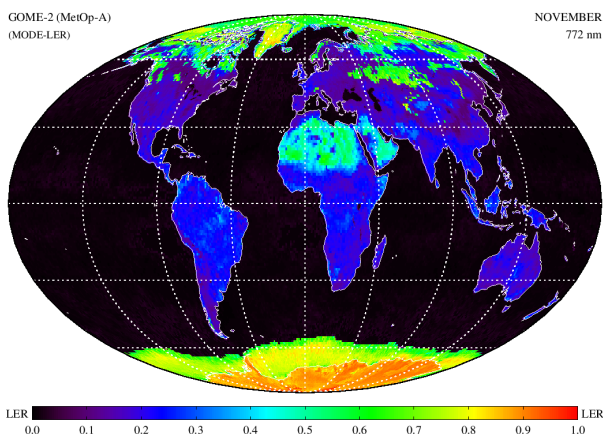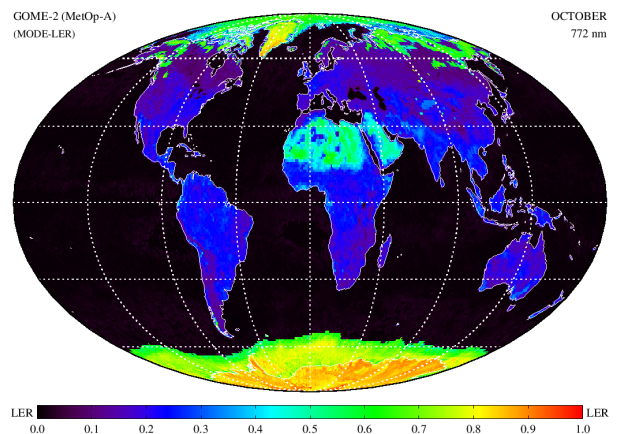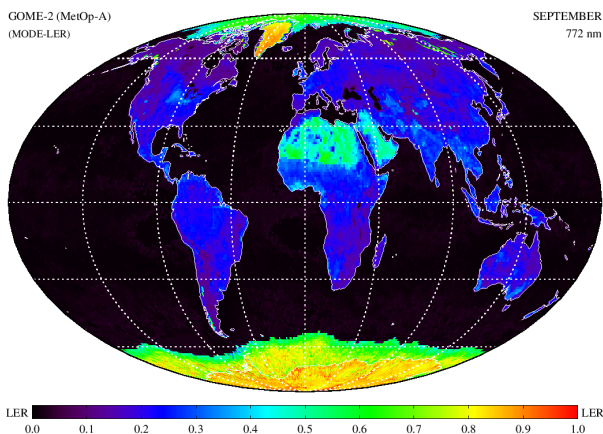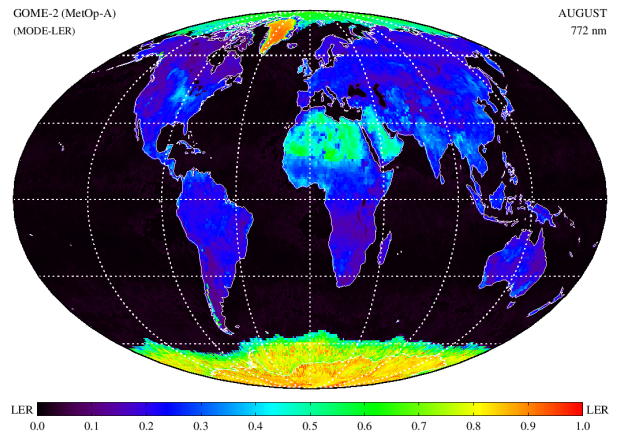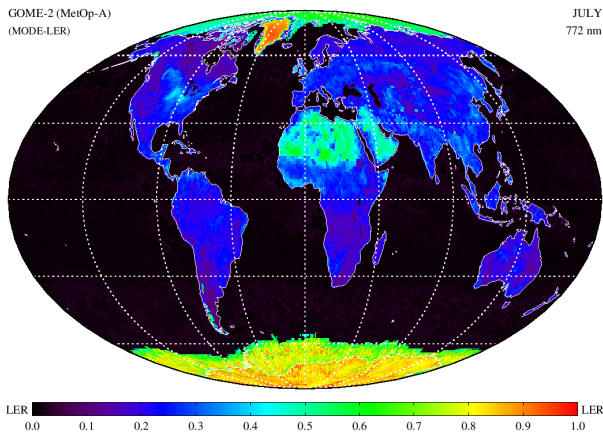
A   Examples of the monthly GOME-2 surface LER product

The following figures present global maps of the GOME-2 surface LER (MODE-LER approach) retrieved at 772 nm for the months January to December. (Continued on next page.)
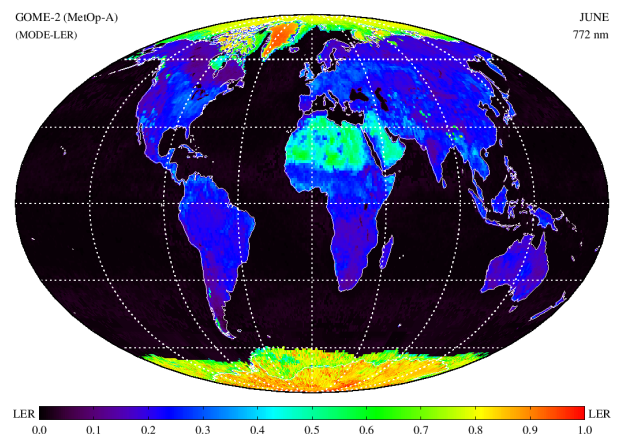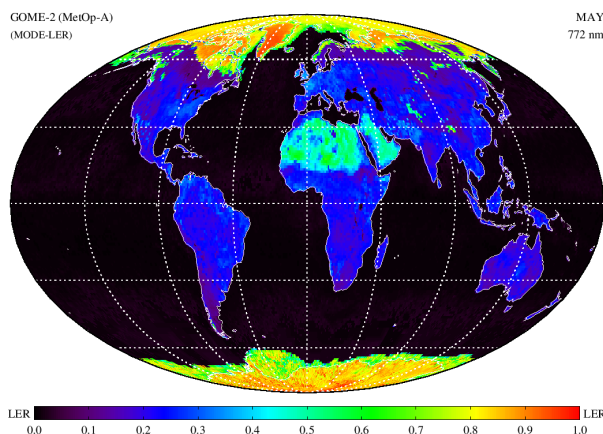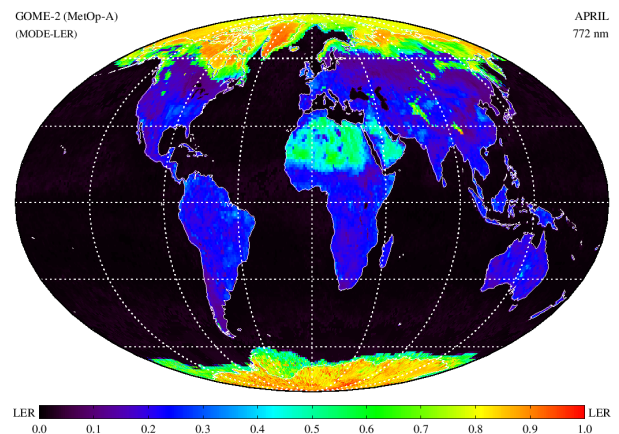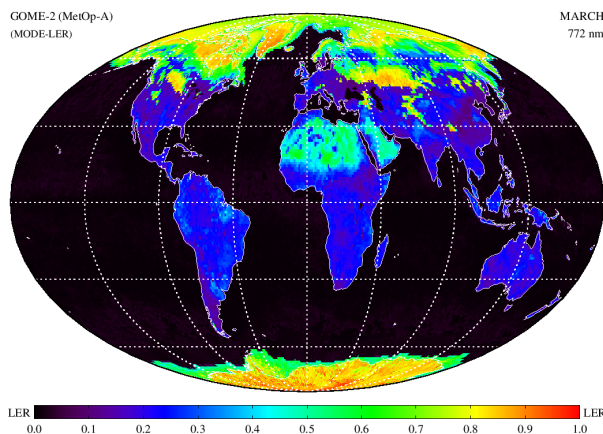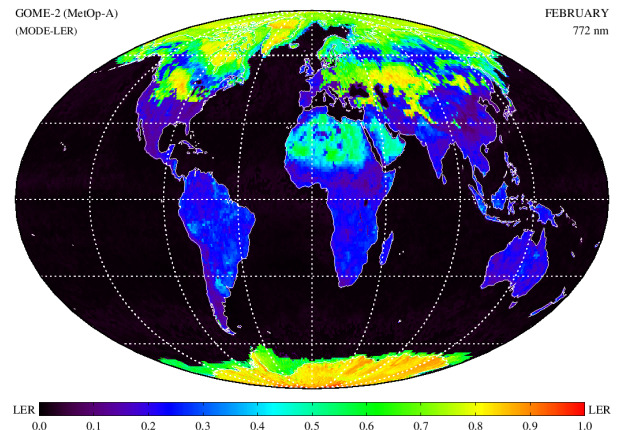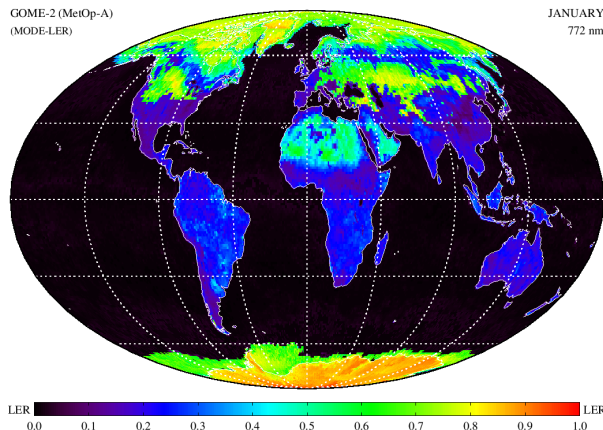
(Continued from previous page.)

B   Overview of solar eclipse events

The following two tables provide an overview of the major solar eclipse events that have occurred since the launch of MetOp-A and MetOp-B. The second column lists the dates on which the solar eclipse events occurred. The third and fourth columns together define the time intervals in which the measurements were noticeably affected. Data in these time intervals are not used.

satellite	date	start time	end time
MetOp-A	19-03-2007	02:48:52 UTC	03:05:09 UTC
MetOp-A	11-09-2007	11:17:10 UTC	11:23:52 UTC
MetOp-A	11-09-2007	12:51:33 UTC	13:06:19 UTC
MetOp-A	07-02-2008	03:11:08 UTC	03:21:21 UTC
MetOp-A	01-08-2008	03:16:39 UTC	03:22:45 UTC
MetOp-A	01-08-2008	08:18:26 UTC	08:24:26 UTC
MetOp-A	01-08-2008	09:59:50 UTC	10:20:20 UTC
MetOp-A	01-08-2008	11:42:59 UTC	11:49:24 UTC
MetOp-A	01-08-2008	13:24:03 UTC	13:30:31 UTC
MetOp-A	01-08-2008	15:04:20 UTC	15:13:01 UTC
MetOp-A	26-01-2009	05:55:33 UTC	06:10:45 UTC
MetOp-A	22-07-2009	01:07:56 UTC	01:23:31 UTC
MetOp-A	15-01-2010	05:19:17 UTC	05:33:47 UTC
MetOp-A	11-07-2010	17:50:19 UTC	18:02:31 UTC
MetOp-A	04-01-2011	08:00:51 UTC	08:18:07 UTC
MetOp-A	25-11-2011	06:38:19 UTC	06:48:26 UTC
MetOp-A	20-05-2012	14:46:28 UTC	14:53:47 UTC
MetOp-A	20-05-2012	16:28:10 UTC	16:35:10 UTC
MetOp-A	20-05-2012	18:09:10 UTC	18:15:10 UTC
MetOp-A	20-05-2012	23:26:31 UTC	23:41:02 UTC
MetOp-A	13-11-2012	21:05:02 UTC	21:22:45 UTC
MetOp-A	09-05-2013	23:16:45 UTC	23:35:28 UTC
MetOp-A	03-11-2013	11:38:12 UTC	11:56:10 UTC
MetOp-A	29-04-2014	04:16:10 UTC	04:23:05 UTC
MetOp-A	23-10-2014	21:09:51 UTC	21:23:16 UTC
MetOp-A	20-03-2015	09:57:13 UTC	10:13:58 UTC
MetOp-A	13-09-2015	06:05:18 UTC	06:18:25 UTC
MetOp-A	09-03-2016	01:02:19 UTC	01:18:35 UTC
MetOp-A	01-09-2016	07:10:12 UTC	07:26:21 UTC

MetOp-A	26-02-2017	12:42:51 UTC	12:54:12 UTC
MetOp-A	21-08-2017	16:43:30 UTC	16:52:37 UTC
MetOp-A	11-08-2018	06:00:00 UTC	24:00:00 UTC
MetOp-A	12-08-2018	00:00:00 UTC	18:00:00 UTC

Table 5: Solar eclipse events since the launch of MetOp-A. Given are the date and the time interval in which the measurements were noticeably affected.

satellite	date	start time	end time
MetOp-B	09-05-2013	22:32:29 UTC	22:52:41 UTC
MetOp-B	03-11-2013	10:55:02 UTC	11:04:14 UTC
MetOp-B	29-04-2014	05:06:27 UTC	05:18:55 UTC
MetOp-B	23-10-2014	20:23:24 UTC	20:35:23 UTC
MetOp-B	20-03-2015	09:15:23 UTC	09:32:35 UTC
MetOp-B	20-03-2015	10:49:31 UTC	10:58:55 UTC
MetOp-B	13-09-2015	07:06:24 UTC	07:17:31 UTC
MetOp-B	09-03-2016	00:17:31 UTC	00:33:49 UTC
MetOp-B	01-09-2016	08:01:54 UTC	08:19:56 UTC
MetOp-B	26-02-2017	13:34:21 UTC	13:58:24 UTC
MetOp-B	21-08-2017	17:29:51 UTC	17:47:36 UTC
MetOp-B	15-02-2018	20:09:15 UTC	20:15:46 UTC
MetOp-B	11-08-2018	08:03:23 UTC	08:11:41 UTC
MetOp-B	11-08-2018	09:44:23 UTC	09:58:12 UTC

Table 6: Solar eclipse events since the launch of MetOp-B. Given are the date and the time interval in which the measurements were noticeably affected.

References

Anderson, G. P., S. A. Clough, F. X. Kneizys, J. H. Chetwynd, and E. P. Shettle (1986), AFGL atmospheric constituent profiles (0–120 km), *Environ. Res. Pap. 954, Rep. AFGL-TR-86-0110*, Air Force Geophys. Lab., Hanscom AFB, Mass.

Burrows, J. P., et al. (1999), The Global Ozone Monitoring Experiment (GOME): Mission concept and first scientific results, *J. Atmos. Sci., 56*(2), 151–175.

Chandrasekhar, S. (1960), *Radiative Transfer*, Dover, Mineola, N. Y., 393p.

de Haan, J. F., P. B. Bosma, and J. W. Hovenier (1987), The adding method for multiple scattering calculations of polarized light, *Astron. Astrophys., 183*, 371–391.

EUMETSAT (2015), GOME-2 Factsheet, Doc. No. EUM/OPS/DOC/10/1299, Issue 4b, 17 March 2015, EUMETSAT, Darmstadt, Germany.

Gao, F., C. B. Schaaf, A. H. Strahler, A. Roesch, W. Lucht, and R. Dickinson (2005), MODIS bidirectional reflectance distribution function and albedo Climate Modeling Grid products and the variability of albedo for major global vegetation types, *J. Geophys. Res., 110*, D01104, doi:10.1029/2004JD005190.

Heath, D. F., A. J. Krueger, H. A. Roeder, and B. D. Henderson (1975), The Solar Backscatter Ultraviolet and Total Ozone Mapping Spectrometer (SBUV/TOMS) for NIMBUS G, *Opt. Eng., 14*(4), 144323, doi:10.1117/12.7971839.

Herman, J. R., and E. A. Celarier (1997), Earth surface reflectivity climatology at 340–380 nm from TOMS data, *J. Geophys. Res., 102*(D23), 28,003–28,011, doi:10.1029/97JD02074.

Kleipool, Q. L., M. R. Dobber, J. F. de Haan, and P. F. Levelt (2008), Earth surface reflectance climatology from 3 years of OMI data, *J. Geophys. Res., 113*, D18308, doi:10.1029/2008JD010290.

Koelemeijer, R. B. A., J. F. de Haan, and P. Stammes (2003), A database of spectral surface reflectivity in the range 335–772 nm derived from 5.5 years of GOME observations, *J. Geophys. Res., 108*(D2), 4070, doi:10.1029/2002JD002429.

Levelt, P. F., G. H. J. van den Oord, M. R. Dobber, A. Mälkki, H. Visser, J. de Vries, P. Stammes, J.O.V. Lundell, and H. Saari (2006), The Ozone Monitoring Instrument, *IEEE Trans. Geosci. Remote Sens., 44*(5), 1093–1101, doi:10.1109/TGRS.2006.872333.

Nicodemus, F. E., J. C. Richmond, J. J. Hsia, I. W. Ginsberg, and T. Limperis (1992), Geometrical Considerations and Nomenclature for Reflectance, in *Radiometry*, edited by L. B. Wolff, S. A. Shafer, and G. Healey, pp. 94–145, Jones and Bartlett Publishers, Inc., USA.

Nolin, A. W., R. L. Armstrong, and J. Maslanik (1998), Near-Real-Time SSM/I-SSMIS EASE-Grid Daily Global Ice Concentration and Snow Extent, 2007–2012, National Snow and Ice Data Center, Boulder, Colorado, USA. Digital media, updated daily.

Popp, C., P. Wang, D. Brunner, P. Stammes, Y. Zhou, and M. Grzegorski (2011), MERIS albedo climatology for FRESCO+ O2 A-band cloud retrieval, *Atmos. Meas. Tech., 4*, 463–483, doi:10.5194/amt-4-463-2011.

Schaaf, C., and Z. Wang (2015), MCD43C1 MODIS/Terra+Aqua BRDF/AlbedoModel Parameters Daily L3 Global 0.05Deg CMG V006, distributed by NASA EOSDIS Land Processes DAAC, doi:10.5067/MODIS/MCD43C1.006.

Stammes, P. (2001), Spectral radiance modelling in the UV-visible range, in *IRS 2000: Current Problems in Atmospheric Radiation*, edited by W. L. Smith and Y. M. Timofeyev, pp. 385–388, A. Deepak, Hampton, Va.

Tilstra, L. G., M. de Graaf, I. Aben, and P. Stammes (2012a), In-flight degradation correction of SCIAMACHY UV reflectances and Absorbing Aerosol Index, *J. Geophys. Res., 117*, D06209, doi:10.1029/2011JD016957.

Tilstra, L. G., O. N. E. Tuinder, and P. Stammes (2010), GOME-2 Absorbing Aerosol Index: statistical analysis, comparison to GOME-1 and impact of instrument degradation, in *Proceedings of the 2010 EUMETSAT Meteorological Satellite Conference*, EUMETSAT P.57, ISBN 978-92-9110-089-7, Cordoba, Spain.

Tilstra, L. G., O. N. E. Tuinder, and P. Stammes (2012b), Introducing a new method for in-flight degradation correction of the Earth reflectance measured by GOME-2, and application to the AAI, in *Proceedings of the 2012 EUMETSAT Meteorological Satellite Conference*, EUMETSAT P.61, Sopot, Poland.

Tilstra, L. G., O. N. E. Tuinder, P. Wang, and P. Stammes (2017), Surface reflectivity climatologies from UV to NIR determined from Earth observations by GOME-2 and SCIAMACHY, *J. Geophys. Res. Atmos., 122*, 4084–4111, doi:10.1002/2016JD025940.

U.S. Department of Commerce, National Oceanic and Atmospheric Administration, National Geophysical Data Center (2006), *2-minute Gridded Global Relief Data (ETOPO2v2)*, http://www.ngdc.noaa.gov/mgg/fliers/06mgg01.html

Wessel, P., and W. H. F. Smith (1996), A global, self-consistent, hierarchical, high-resolution shoreline database, *J. Geophys. Res., 101*(B4), 8741–8743, doi:10.1029/96JB00104.